

2

Radiation Environments

2.1 Introduction

This chapter provides a brief introduction to the various radiation environments that may be encountered by electronic systems and components. In the first part of the chapter, some basic sources of radiation are reviewed, including atomic and nuclear processes such as radioactive decay. Sections 2.2 and 2.3 provide a good physics background for the deeper dive into fundamental radiation effects discussed in Chapters 3 and 4. We then discuss the three predominant natural sources of radiation in the space environment and the man-made environments found in commercial nuclear reactors, nuclear weapons scenarios, and high-energy physics facilities.

2.2 X-Rays, Gamma Rays, and the Atom

As a first step in understanding actual radiation environments, we examine some of the physical processes that give rise to radiation. These include atomic as well as nuclear scale events like radioactive decay. An obvious prerequisite for the following discussion is a good working knowledge of the atomic shell structure and the quantum mechanics behind this structure. The introduction provided in Chapter 1 as well as the problems at the end of Chapter 1 are good starting points for this knowledge.

2.2.1 X-Rays

The discovery of X-rays, attributed to Wilhelm Röntgen in 1895, came after numerous researchers noted odd effects while experimenting with cathode ray tubes. Crookes and Hitton noted fogging of photographic plates near their cathode ray apparatus in the 1880s, but many experimenters from about 1877 up through 1895 studied X-rays and noted such effects. The name “X-ray” comes from Röntgen’s naming of the radiation, denoting its unknown nature.

The most familiar sources of X-rays are modern versions of early tubes, such as in Figure 1.2. An example output from an X-ray tube is shown in Figure 2.1. The X-rays produced consist of a continuous spectrum of wavelengths with the shortest wavelength (cutoff frequency) corresponding to the applied anode voltage. The broad range of X-ray wavelengths from an X-ray tube is the result of electron bremsstrahlung. Bremsstrahlung, or braking radiation, results when an electron comes close enough

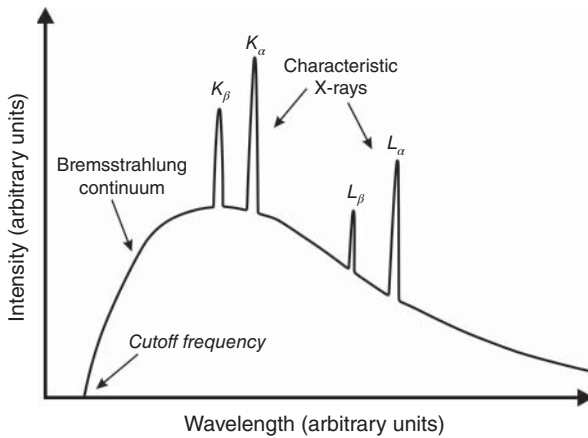


Figure 2.1 Output from an X-ray tube showing characteristic and bremsstrahlung components.

to a nucleus of an atom to cause a change in the electron velocity. As explained more thoroughly in Chapter 3, an accelerating electron will radiate. In an X-ray tube, the applied anode voltage establishes the maximum electron energy so that the shortest wavelength X-ray (highest energy) is produced when the electron loses all of its kinetic energy to bremsstrahlung.

The spectrum in Figure 2.1 also includes several characteristic X-ray spectral lines that depend on the anode material of the X-ray tube. The characteristic spectral lines are from X-ray fluorescence. In X-ray fluorescence, electrons with enough energy can displace an inner-shell electron from an anode metal atom and the resulting vacancy is filled by a higher-energy-shell electron. The energy difference between the shells is released as an X-ray photon with a characteristic frequency (Eq. (1.2)). The K_α and K_β lines are from $L \rightarrow K$ and $M \rightarrow K$ transitions, respectively, and are the most prominent lines. There may also be L_α and L_β lines in the X-ray tube output and these are X-rays from $M \rightarrow L$ and $N \rightarrow L$ shell transitions (either cascade fill-in from prior K-shell vacancies or L-shell electrons removed by an incident electron).

The displaced shell electron is called a secondary electron. Incident and secondary electrons will undergo elastic and inelastic interactions in the anode, losing their energy through fluorescence and bremsstrahlung radiation until they thermalize. Figure 2.2 provides a diagram for the X-ray fluorescence and bremsstrahlung radiation production. The removal of the k-shell electron e_k by an incident electron e_1 shown in Figure 2.2a leads to the emission of X-ray photon γ_1 in Figure 2.2b. The ejected electron is called a secondary electron. Also shown in Figure 2.2b is an incident electron e_2 that emits a photon γ_2 due to bremsstrahlung. Depending on the anode material, transitions involving the filling of empty L-shell as well as empty K-shell electron states may also produce characteristic X-rays. Elements with higher atomic number have more tightly bound inner shell electrons as shown in Figure 2.3 where the electron binding energy versus atomic weight is plotted with electron shell as a parameter. The 1s line corresponds to the K-shell electron. The characteristic X-ray photon energy produced by various anode materials is shown in Table 2.1.

In addition to the familiar man-made variety, there are also many sources of X-rays in space, including stars, galaxy clusters, quasars, black holes, and supernova remnants.

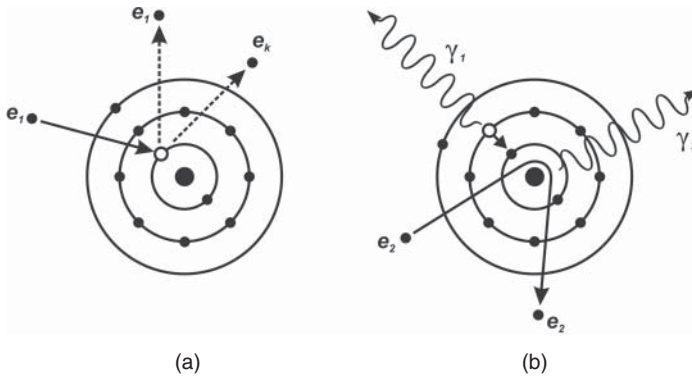


Figure 2.2 X-rays are produced by X-ray florescence and bremsstrahlung. (a) An incident electron e_i removes a K-shell electron e_k . (b) A higher shell electron fills the K-shell vacancy, emitting a characteristic X-ray photon γ_1 . Alternatively, an incident electron e_2 comes close enough to the nucleus to change direction (accelerate) and releases a bremsstrahlung (braking radiation) photon γ_2 .

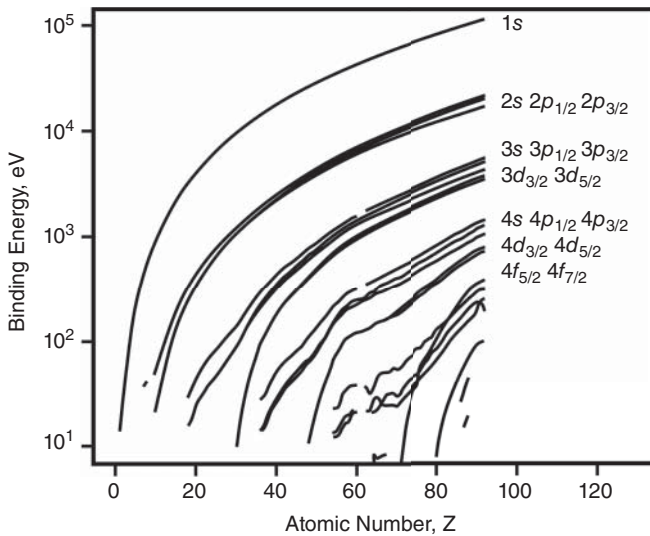


Figure 2.3 Binding energies for shell electrons. Source: Adapted from Thompson 2009 [1], Table 1-1, pp. 1-2 to 1-7.

Some of these are covered in more detail in “The Space Environment” section later in this chapter.

X-rays can be classified by their energy. Soft X-rays range from about 100 eV to 1000 eV whereas hard X-rays have energies from 1000 eV to 200 keV. X-rays with the highest energies (hex-ray) range in energy from 100 keV to 1 MeV. The dividing line between soft and hard X-rays is around 5 keV – 10 keV. While there is some overlap in energy when distinguishing X-rays from gamma rays, as seen in Figure 2.4, there are other factors to consider. For example, X-rays can be considered as originating from interactions at the atomic level and gamma rays from nuclear interaction but this classification ignores stellar bremsstrahlung events that produce gamma rays. There

Table 2.1 K-shell emission line energy for various X-ray tube anode materials.

Anode material	Atomic number	K-shell photon energy (keV)	
		K _{α1}	K _{β1}
Cu	29	8.05	8.91
Ga	31	9.25	10.26
Mo	42	17.5	19.6
Ag	47	22.2	24.9
In	49	24.2	27.3
W	74	59.3	67.2

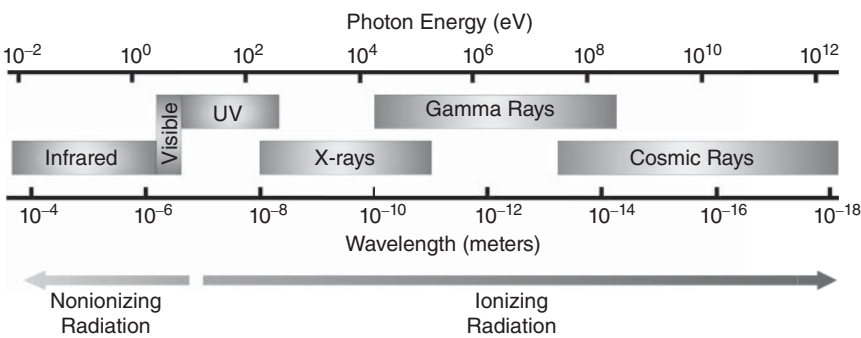


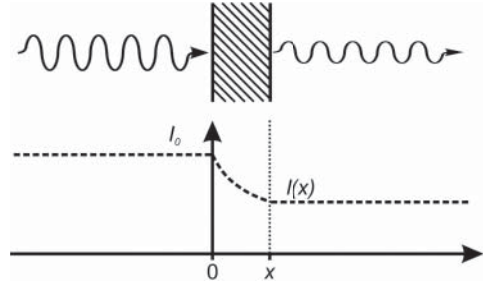
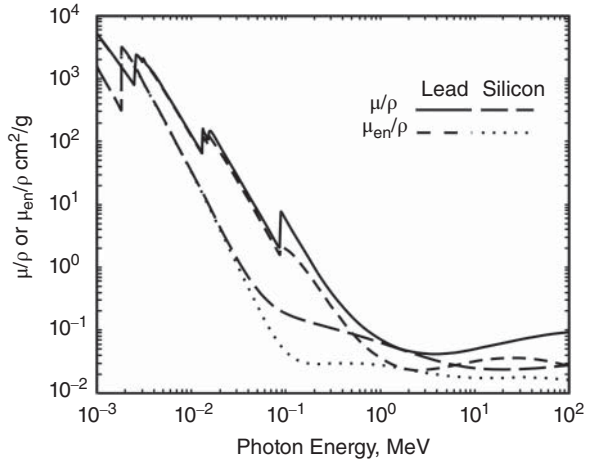
Figure 2.4 Portion of the electromagnetic spectrum showing the energy ranges of ionizing radiation.

may also be an historical aspect for the classification of sources as either X-ray or gamma ray, for example, when a detector did not register wavelength information. In general, the division can be in terms of energy, but one term or another can be used to preserve the historical context.

2.2.2 X-Ray Absorption

It is well known that X-rays have an ability to penetrate materials that are opaque to lower energy radiation. This ability is due to the small wavelength of X-ray radiation. The photon energy of less energetic radiation such as visible, ultraviolet, and infrared is absorbed through an energy transfer to electronic, vibrational, and rotational energy states in the material, but X-ray photons have energy levels that are several orders of magnitude larger than visible radiation. They are very unlikely to interact through low energy transfer processes. If they interact electronically with the material, it is with the tightly bound K- or L-shell electrons in the atoms of the heavier elements, so clearly X-rays will readily penetrate most materials.

The absorption of X-ray photons in a material can be derived for the simple case of a beam of monotonic X-rays that are incident on an absorber, as shown in Figure 2.5. A reduction in intensity occurs as the X-ray beam traverses the material that is proportional to the thickness of the material as well as the absorption property of the material.

Figure 2.5 X-ray absorption diagram.**Figure 2.6** Comparison of the mass attenuation coefficients for lead and silicon. Source: Adapted from Hubbell and Seltzer 2004 [2], <http://physics.nist.gov/xaamdi>.

Over a small increment dx the intensity will be reduced by

$$dI = -\mu I dx. \quad (2.1)$$

Solutions to Eq. (2.1) have the form of an exponential decay

$$I = I_0 e^{-\mu x} \quad (2.2)$$

where I_0 is the initial intensity and μ is usually called the linear absorption coefficient (but macroscopic absorption coefficient or linear attenuation coefficient are also used). It is common to normalize the linear absorption coefficient to the density of the material, μ/ρ , and this quantity is called the mass attenuation coefficient.

The quantities μ and μ/ρ are dependent on the frequency of the X-rays because the absorption in a material will depend on the energy states of the bound electrons. Light elements may have only K-shell electrons that can absorb an X-ray photon's energy, with an uptick in the absorption at a relatively low photon energy corresponding to the K-shell to L-shell electron transition. Heavier elements will have several electron shell transitions that can contribute to the absorption of X-ray photon energy. Figure 2.6 provides a comparison of the mass attenuation coefficients for lead and silicon as a function of the X-ray photon energy. The mass energy absorption coefficient μ_{en}/ρ is also shown in Figure 2.6. This quantity removes the fraction of the energy of secondary charged particles that is lost to bremsstrahlung in the material from the calculation for the absorption coefficient.

The sharp transition in absorption occurs for photon energies that are equal to the binding energy of an electron shell in the absorber material. These transitions are called absorption edges or critical excitation energies. The primary absorption mechanism for lower-energy X-rays is the photoelectric effect, but other absorption processes also occur at low photon energy, including Compton scattering (or incoherent scattering) and Thomson scattering. At higher photon energies, pair production and photodisintegration contribute to photon energy loss. These effects are explored more thoroughly in Chapter 3.

2.2.3 Auger Electrons

A variant of the K-shell ejection process shown in Figure 2.2 produces an electron instead of a photon. The electron is called an Auger electron and is named after Pierre Auger, a French physicist who shares his discovery of the effect in 1923 with Austrian-Swedish physicist Lise Meitner, who independently discovered the effect in 1922. As shown in Figure 2.7, an electron dislodges an inner shell electron of an atom, but the energy released when the shell vacancy is filled is transferred to another electron in the same atom. This electron is ejected from the atom with energy that is equal to the orbital binding energy of the electron and the difference in the inner shell electron energies:

$$E = E_2 - E_1 + E_{\text{core}}. \quad (2.3)$$

The resultant atom has two electron vacancies in its electron shell.

The Auger effect has been used since the mid-1950s to analyze the chemical composition of surfaces and has wide application in the microelectronics industry. Sometimes the energy release from an inner electron shell vacancy filling is shared between the emission of an X-ray photon and the simultaneous promotion of an electron into either a bound or a continuum state. This process is called the radiative Auger effect and was discovered by F. Bloch and P. A. Ross in 1935.

2.2.4 Nuclear Structure and Binding Energy

We now turn to radiation that has its origins in the nucleus of atoms. Scattering experiments suggest that nuclei are roughly spherical and appear to have the same density

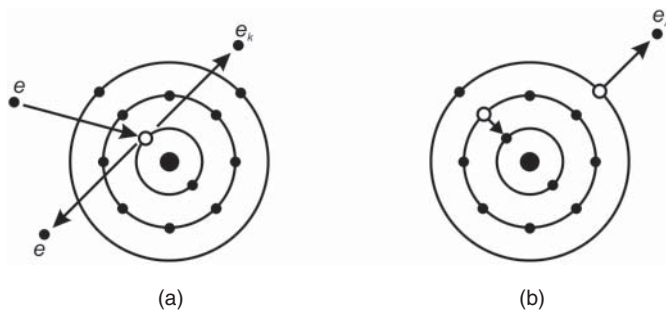


Figure 2.7 Diagram of the Auger effect. (a) An incident electron e scatters a K-shell electron e_k . (b) An L-shell electron fills the K-shell vacancy and an outer electron e_A is ejected.

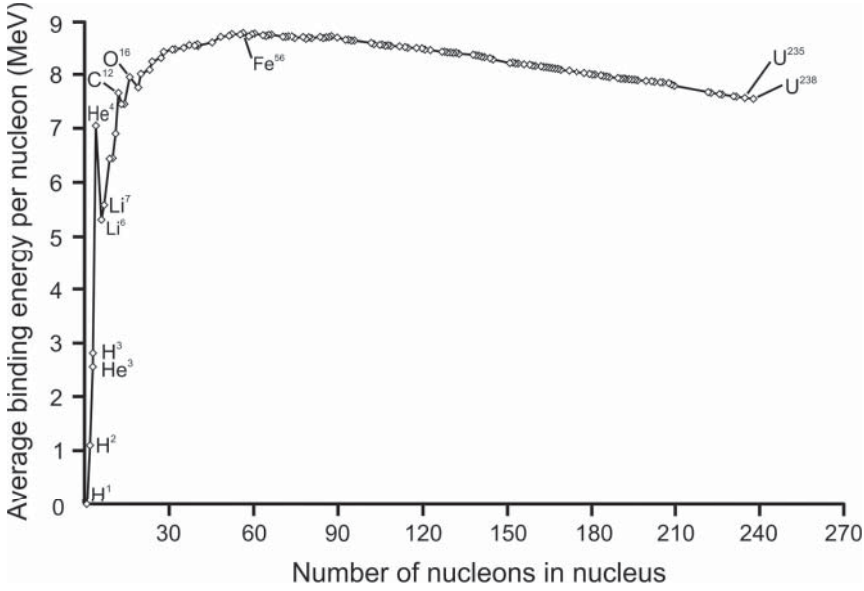


Figure 2.8 Nuclear binding energy versus nucleon.

regardless of atomic mass number A . The nuclear radius is given by the Fermi model

$$R = r_0 A^{1/3}, \quad (2.4)$$

where $r_0 = 1.25\text{--}1.5\text{ fm}$.

The energy required to remove one nucleon from a nucleus is called the average binding energy per nucleon. Measurements of this energy per nucleon indicate a range between 7 MeV to about 9 MeV for most elements, as shown in Figure 2.8. This is a million times higher than the ionization energy, the energy required to move a bound electron to infinity, or 25 eV or less for most elements [3]. Nuclear binding energies are highest near iron, making the nuclei of ${}^{56}\text{Fe}$, ${}^{58}\text{Fe}$, and ${}^{62}\text{Ni}$ the most stable of all elements. In fact, if one assumes the reaction must be exoergic, fission and fusion events are sharply divided around iron with fusion energetically favored for elements lighter than iron and fission favored for elements heavier than iron.

When nucleons combine into a nucleus, they lose energy so that the resultant nucleus has a smaller mass than its constituent nucleons. The missing mass, known as the mass defect, represents the energy released when the nucleus is formed and is a measure of the binding energy of the nucleus. For this reason, the plot in Figure 2.8 is sometimes called the mass defect curve. The mass defect was first noted by British chemist and physicist Francis William Aston in 1920. If $M(N, Z)$ is the nuclear mass of an element and N and Z are the neutron number and atomic number, respectfully,

$$M(N, Z) = ZM_H + NM_n - E_B \quad (2.5)$$

where M_H is the mass of the hydrogen nucleus, M_n is the mass of the neutron, and E_B is the binding energy of the nucleus. Note that E_B in Eq. (2.5) is a measure of the total binding energy and not the binding energy per nucleon as in Figure 2.8.

2.2.4.1 Models of the Nucleus

Over the years, various models have been proposed to describe nuclear structure, but there is no one model that fits all of the observed nuclear properties. While it is understood that there is strong binding between nucleons related to the strong force, this interaction is provided in some models via a central nuclear field or potential so that there is weak or no nucleon–nucleon interaction as such. These models can be referred to as central field or microscopic models where the nucleons rarely interact with each other like the molecules in a gas. Other models provide for strong nucleon–nucleon interaction so that the nucleus behaves like a liquid or a solid. These models are called collective or strong nuclear force models.

2.2.4.1.1 Liquid Drop Model The liquid drop model was first proposed by George Gamow in 1928 [4], and Gamow's analysis inspired Heisenberg (1933) and Weizsacker (1935) to study the mass defect curve (Figure 2.8). Gamow's nuclear model grouped the nucleons into N alpha particles, but in a more modern version of the liquid drop model, the semiempirical mass formula, protons and neutrons interact with each other at a short range through the strong force. This is similar to the way that water molecules are attracted to each other under the short-range van der Waals force. The liquid drop model uses this similarity to describe the nucleus as a classical fluid made up of protons and neutrons with an internal repulsive electrostatic force proportional to the number of protons [5]. In Bohr's concept of the compound nucleus in nuclear reactions, interactions between the particles in the nucleus are strong so that particles do not behave independently of each other. The energy of an incident particle that is captured by the nucleus is quickly shared by the other nucleons [6]. Furthermore, captured particles have a mean free path that is much smaller than the diameter of the nucleus.

Semiempirical mass formulas describe the binding energy E_B in Eq. (2.5) as the sum of a series of terms, each of which represent some aspect of the nucleus:

$$E_B = E_V + E_S + E_C + E_A + E_P + \dots \quad (2.6)$$

While some mass formulas may have hundreds of terms, the first several terms are most important and provide an accurate model for the binding energy. The first term in Eq. (2.6), E_V , represents a volume energy or exchange energy. It is the energy lowering that occurs due to the potential well created by the attractive strong force and is expected to be proportional to the number of nucleons:

$$E_V = a_0 A. \quad (2.7)$$

The constant a_0 is evaluated empirically. For very large A , such as inside a neutron star where $A \rightarrow \infty$ and there are few protons, E_V would be the only major term in Eq. (2.6). Nuclei are small, however, and bounded by a surface where nucleons see lower exchange energy with their neighbors. We expect a deficit of binding energy for these surface nucleons and deduct a correction term E_S for nucleons at the nuclear surface

$$E_S = -a_1 A^{2/3}. \quad (2.8)$$

As with the volume term, the constant a_1 in the surface term is evaluated empirically. Coulomb repulsion between protons is the only long-range force in the nucleus. We can regard the total nuclear charge of Ze as spread uniformly throughout the nuclear volume. This leads to a loss in binding energy E_C due to the Coulomb repulsion:

$$E_C = -a_2 \frac{Z(Z-1)}{A^{1/3}} \quad (2.9)$$

with the constant a_2 evaluated from empirical data and noting that the Coulomb interaction is between a single proton in the nucleus and the $Z - 1$ remaining protons.

According to Raoult's law, in any two-component liquid with nonpolar attractive forces, the minimum energy occurs when the two components are in equal concentrations. This effect is modeled in nuclei by an asymmetry term E_A given by

$$E_A = -a_3 \frac{(A - 2Z)^2}{A} \quad (2.10)$$

where the constant a_3 is evaluated from empirical data. The asymmetry term takes into account a composition effect in the nucleus. The maximum stability is achieved when there are an equal number of protons and neutrons. When there are excess neutrons, they occupy higher energy states than if paired with a proton, so excess neutrons are not as tightly bound in the nucleus. The E_A term subtracts from binding energy in Eq. (2.6) when there is an imbalance between proton and neutron number.

A final term in Eq. (2.6), E_p , represents an energy correction due to pairing of protons and pairing of neutrons. Pairing of proton with proton lowers energy through the Pauli exclusion principle when the number of spin-up protons is equal to the number of spin-down protons. The same is true for neutrons in the nucleus. The pairing term has an effect like the asymmetry term but has three possible settings. When there are an even number of protons and an even number of neutrons (e-e), the pairing term is additive to Eq. (2.6). If there is an even number of protons but the neutron number is odd, the term is zero. The term is also zero if neutron number is even and proton number is odd (e-o and o-e). When both proton and neutron number are odd, the term subtracts from Eq. (2.6) (lowers binding energy). The pairing term E_P in Eq. (2.6) is given by

$$E_p = -a_4 \frac{\delta}{A^{1/2}}, \quad \text{where } \delta = \begin{cases} +1 & \text{for e - e} \\ 0 & \text{for e - o and o - e} \\ -1 & \text{for o - o} \end{cases} \quad (2.11)$$

As with the other terms, there is a fitting parameter, a_4 , which is determined empirically. The final form of the semiempirical mass formula is

$$E_B = a_0 A - a_1 A^{2/3} - a_2 \frac{Z(Z-1)}{A^{1/3}} - a_3 \frac{(A-2Z)^2}{A} - a_4 \frac{\delta}{A^{1/2}}. \quad (2.12)$$

Equation (2.12) provides a prediction of binding energy for heavier nuclei and can be accurate to about 1% for nuclei with $A > 40$. Some published values for the fitting parameters $a_0 - a_4$ in the semiempirical mass formula are provided in Table 2.2 and

Table 2.2 Comparison of fitting parameters for the semiempirical mass formula.

Reference	Volume	Surface	Coulomb	Asymmetry	Pairing
1936 Bethe and Bacher [7]	13.86	13.2	0.58	19.5	
1945 Fermi [8, 9]	14.0	13.0	0.583	19.3	$33.5/A^{3/4}$
1955 [5]	14.1	13	0.595	19.0	(Graph)
2004 [10]	15.19	16.51	0.675	20.72	12.53

Source: Adapted from Evans 1955 [5], table 3.3, p. 383.

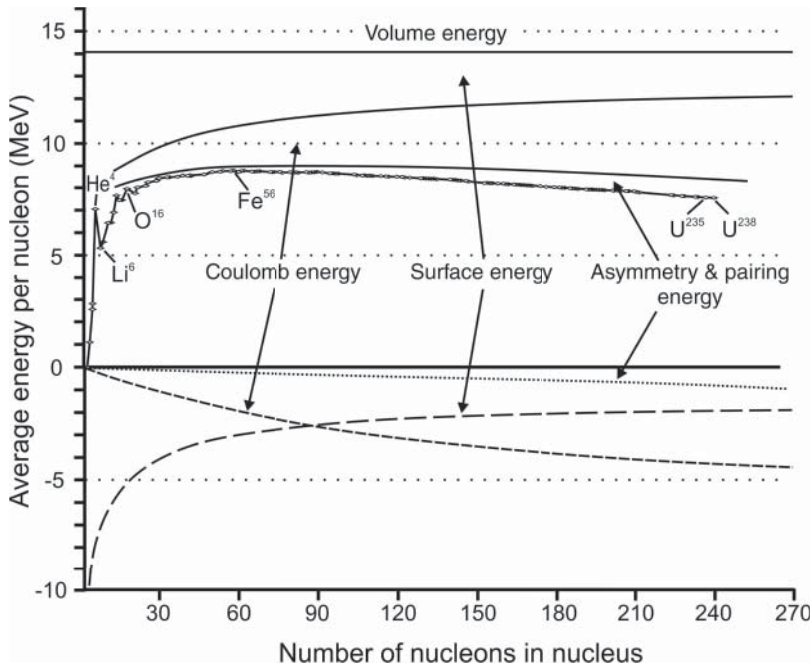


Figure 2.9 Nuclear binding energy showing the various energy components in the semiempirical mass formula. The net binding energy from the formula (not shown for clarity) aligns approximately with the actual binding energies for the heavier nuclei. The surface, Coulomb, and asymmetry energies subtract from the volume energy and are plotted separately in the lower part of the graph.

can also be found in [11–14]. Figure 2.9 shows the relative contributions of the various energy terms (with $a_0 = 14.1$ MeV) to the binding energy. Note that the influence of the surface and Coulomb terms are primarily responsible for the peak in binding energy around iron.

In spite of the different approaches taken by the various contributors, Eq. (2.12) gives an accurate match for the behavior of many elements and isotopes. For lighter nuclei, Eq. (2.12) is not a good predictor of binding energy, especially ${}^4\text{He}$, mainly because the model doesn't consider internal structure of the nucleus and fails to predict the observed nuclear shell behavior. Modeled as an incompressible fluid, the ground state energies for the nucleus are accurately predicted, but excited states must be visualized as vibrational modes or nuclear surface vibrations corresponding to periodic deformations of the nuclear “droplet.” The lowest permissible mode of surface vibration corresponds to excitation energy many times greater than the lowest observed excitation energy of the nucleus [15]. Still, the liquid drop model and nuclear models based on the concepts of the liquid drop model provide valuable insights into the possible energy states that could lead to nuclear fission and other nuclear events [16].

2.2.4.1.2 Fermi Gas Model The Fermi gas model was an early attempt to add quantum mechanics into the nuclear model, mainly through a statistical treatment. Protons and neutrons are fermions, so they will obey Fermi-Dirac statistics in the nucleus. Fermions obey the Pauli exclusion principle, so energy states in the nucleus are filled from the lowest energy state upward with each energy state accommodating a spin-up and spin-down particle. Nucleons move freely in a nuclear potential well, which is due to the influence of all nucleons and has as a first estimate a rectangular shape. Neutrons and protons experience different potential wells in the nucleus, however.

In addition to the potential created by the strong force, protons are affected by the Coulomb force. This causes the neutron potential well to be deeper than the proton potential well so that protons are less tightly bound in the nucleus than neutrons.

Since the nucleons are noninteracting and have only kinetic energy, the model is that of two Fermi gases, one proton and one neutron, occupying the same volume. A diagram of the Fermi gas model potential well is shown in Figure 2.10. The energy of the highest occupied state is the Fermi energy and protons and neutrons can be viewed as having separate Fermi energies. Note the Fermi energies are aligned for neutrons and protons in Figure 2.10 and this is the situation for all stable nuclei. If the proton and neutron Fermi energies were not aligned, the nucleus would undergo beta decay (Section 2.2.5.2) in order to establish a more stable condition.

We can estimate the Fermi energy by first calculating the number of nucleon states up to the Fermi energy E_F . Looking at a single dimension we have from the Heisenberg uncertainty principle, the one-dimensional volume of a particle in phase space:

$$\Delta x \Delta p \geq \frac{1}{2} \hbar \Rightarrow 2\pi \hbar. \quad (2.13)$$

The number of nucleon states in a volume V is then just the total number of states in phase space divided by the volume in phase space for one particle:

$$n = \frac{\iint d^3r d^3p}{(2\pi \hbar)^3} = \frac{V \cdot 4\pi \int_0^{p_F} p^2 dp}{(2\pi \hbar)^3} = \frac{V \cdot p_F^3}{6\pi^2 \hbar^3}. \quad (2.14)$$

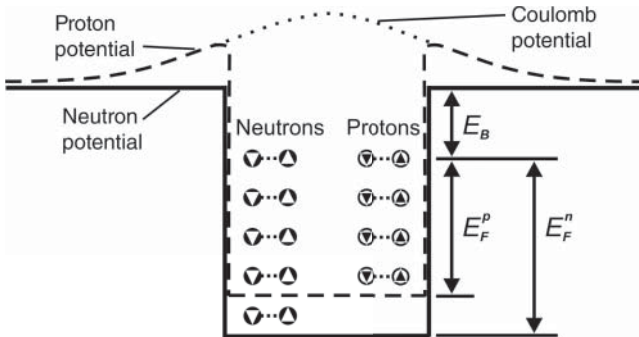


Figure 2.10 Fermi gas model diagram, note that E_B is the binding energy per nucleon.

Note that in Eq. (2.14) the integration over real space yields the volume V whereas the integration over momentum has been converted into spherical coordinates and represents a differential volume of a sphere of radius p from radius p to $p + dp$. Such a region represents an equal energy surface regardless of the direction of p . Given that each state of Eq. (2.14) can hold two fermions of the same species, we have

$$N = \frac{V \cdot (p_F^n)^3}{3\pi^2 \hbar^3} \quad \text{for neutrons and} \quad (2.15)$$

$$Z = \frac{V \cdot (p_F^p)^3}{3\pi^2 \hbar^3} \quad \text{for protons.} \quad (2.16)$$

In Eqs. (2.15) and (2.16) the Fermi momentum for protons and neutrons is designated by the addition of a p or n superscript, respectively. For a nucleus with $N = Z = A/2$ the proton and neutron Fermi energies will be equal. Using Eq. (2.4) we have

$$n = \frac{A}{2} = 2 \cdot \frac{V \cdot p_F^3}{6\pi^2 \hbar^3} = 2 \cdot \frac{4\pi}{3} r_0^3 A \cdot \frac{p_F^3}{6\pi^2 \hbar^3} = \frac{4Ar_0^3 p_F^3}{9\pi \hbar^3} \quad (2.17)$$

and

$$p_F = \left(\frac{9\pi}{8} \right)^{1/3} \cdot \frac{\hbar}{r_0}. \quad (2.18)$$

Using the values of r_0 from Eqs. (2.4) and (2.18) provides a momentum of 240–250 MeV/c for nucleons at the Fermi level, indicating that nucleons move in the nucleus with a high momentum. The corresponding Fermi energy is

$$E_F = \frac{p_F^2}{2M} \approx 33 \text{ MeV} \quad M = 938 \text{ MeV}. \quad (2.19)$$

Given the average binding energy of 7–9 MeV for most elements, Eq. (2.19) predicts a potential well depth of about 41 MeV so that nucleons are, in fact, lightly bound in the nucleus.

Estimating the average nucleon energy can provide some additional insight into elements with unequal proton and neutron numbers, but the Fermi gas model provides no information on the individual nucleon energy levels other than the pairing of fermions in each energy state.

2.2.4.1.3 Shell Model There is a lot of evidence that nuclei have a shell configuration and that nuclei have greater stability when shells are filled or closed. In particular, the stability of atomic nuclei that have either neutron number N or atomic number Z with the magic numbers 2, 8, 20, 28, 50, 82, and 126 has been noted. The influence of these magic numbers is seen in the relative abundance of the Earth's elements as in Figure 2.11 and also can be seen when the lifetime of the various elements and isotopes are plotted versus neutron and atomic number as in Figure 2.12. This plot also shows a deviation away from $Z = N$ for stable elements indicating a need for more neutrons to dilute the effect of the Coulomb repulsion between protons as the nucleus becomes larger. When the neutron cross sections for the various nuclei are examined, those with magic neutron numbers have much lower cross sections by about two orders of magnitude, indicating these nuclei are much less likely to absorb an additional neutron. The electric quadrupole moments for nuclei with magic numbers of neutrons or protons are found to be nearly zero, indicating they are spherically symmetric. It is also worth noting that of the four decay series (Section 2.3.2), three terminate in elements that are singly magic and the fourth terminates in a doubly magic isotope.

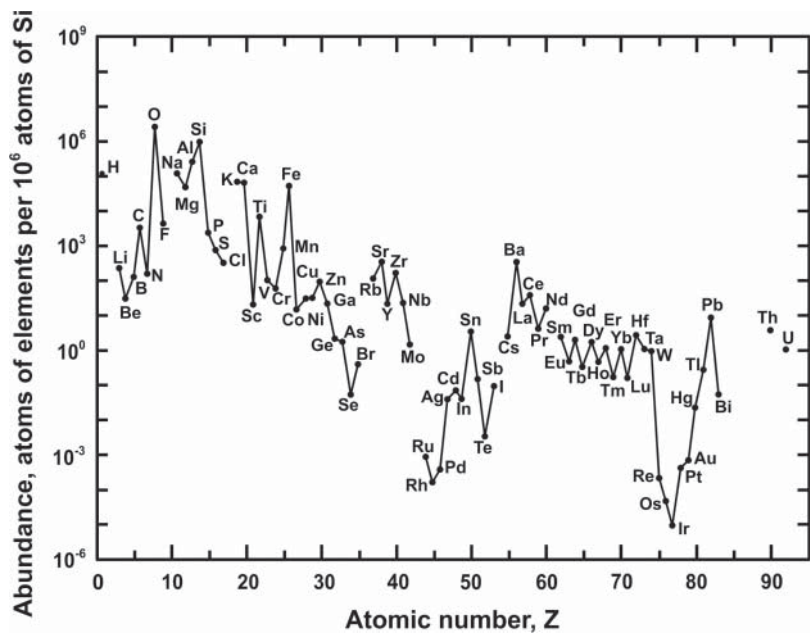


Figure 2.11 Relative abundance of the chemical elements in Earth's upper continental crust (atoms per 10^6 atoms of Si). Source: Adapted from Haxel et al. 2002, U.S. Geological Survey Fact Sheet 087-02, <https://pubs.usgs.gov/fs/2002/fs087-02>, Figure 4 [17].

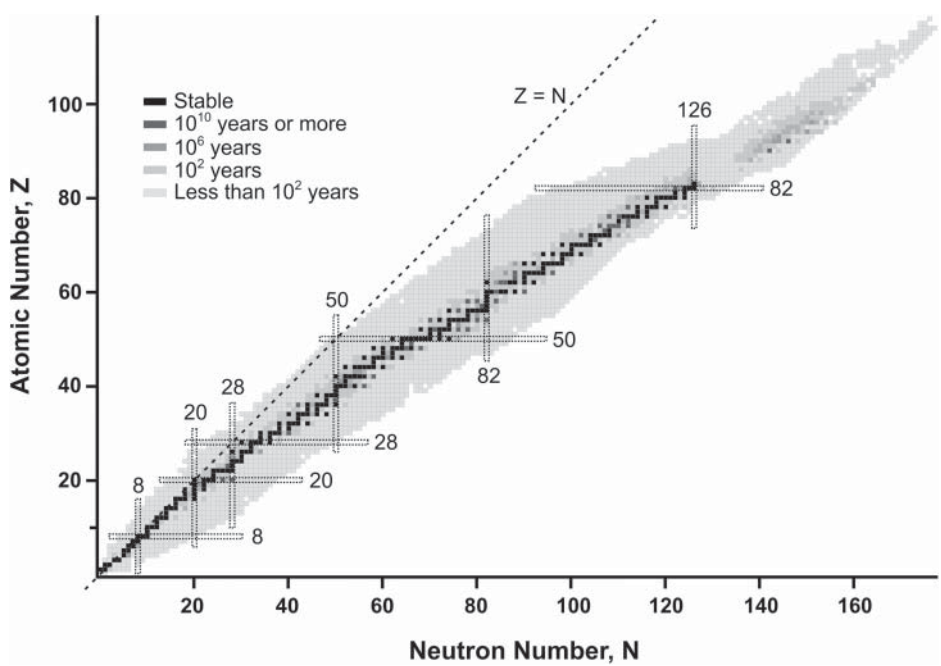


Figure 2.12 Half-life of elements and their isotopes. Source: Adapted from Chart of Nuclides, National Nuclear Data Center, <http://www.nndc.bnl.gov/chart>.

The observation of magic numbers for protons and neutrons and the success of quantum mechanical models for electron shells in atoms provided clues for a similar quantum mechanical treatment of the nucleus. The shell model of the nucleus, developed in 1949, was the result of independent development of earlier shell models (Dmitry Ivanenko and E. Gapon in 1932) by several physicists, including Eugene Paul Wigner, Maria Geoppert-Mayer, and J. Hans D. Jensen. In fact, these three physicists shared the Nobel Prize in 1963 for their contributions to the nuclear shell model.

A shell configuration in the nucleus implies that nucleons are moving in a potential well created by the forces of all of the other nucleons, but what is this potential? We know it isn't the strong force, as this force acts between the quarks in each nucleon. The energy required to separate two quarks far exceeds the creation energy for a quark/anti-quark pair so attempts to isolate individual quarks end up creating other hadrons (either two-quark particles called mesons or three-quark particles called baryons). Quarks carry a color charge, so unlike a Coulomb field that decreases in strength when two electrically charged particles are separated, the force-carrying gluons create a color field that stretches into a narrow tube or string when quarks are separated so that the strength of the force or the color field remains constant. The action of the color field is called color confinement as it keeps the color field from being observed.

What we observe as the binding force between nucleons is a residual strong force that can be thought of as a kind of London dispersion force. While the binding force is much weaker than the strong force binding quarks, it is still much stronger than the Coulomb repulsion and it also retains some features of the strong force. It is highly attractive in the range of 1 fm but becomes repulsive at about 0.7 fm in keeping with the Pauli exclusion principle. The potential drops off rapidly at a distance of about 2.5 fm. In the shell model, one seeks an average or mean potential that models the collective influence of the nucleus on a single nucleon. Simple potentials such as a finite spherical well or a harmonic oscillator well can be used, but the shape of the potential has a large effect on the prediction of the energy states. A typical choice for the potential is the Woods-Saxon potential:

$$V_{WS}(r) = -\frac{V_0}{1 + e^{(r-R)/a}}, \quad (2.20)$$

where the nuclear radius R is provided by Eq. (2.4), the potential well depth $V_0 \approx 60$ MeV and the surface thickness $a \approx 0.65$ fm. This potential has a nearly constant potential near the center when the atomic mass number A is large. For nucleons on the surface of the nucleus (i.e. $r \approx R$) there is an attractive force toward the center of the nucleus and the potential drops to zero as r goes to infinity ($r - R \gg a$). As with the Fermi model, neutrons and protons have independent states that are the result of the different potential wells they occupy. So for protons, a Coulomb potential is added to Eq. (2.20), which extends beyond the nucleus and provides a net repulsive force for protons outside the nucleus.

The solution to Schrodinger's equation using potential fields such as Eq. (2.20) follows the usual route using separation of variables in the proposed wave function:

$$\Psi(r, \theta, \phi) = R(r)\Theta(\theta)\Phi(\phi). \quad (2.21)$$

The spherical symmetry of the potential field makes separation of variables possible, dividing the wave function into radial and harmonic parts. The wave function Ψ represents the physical probability for the location of the particle. As such, it must be single valued and continuous and finite everywhere. This restricts the harmonic functions $\Theta(\theta)$ and $\Phi(\phi)$ to the form

$$\Theta(\theta) = P_l^{(m)}(\cos \theta) \quad (2.22)$$

$$\Phi(\phi) = e^{im\phi} \quad (2.23)$$

where $P_l^{(m)}$ are the associated Legendre polynomials of order l in $\cos\theta$ and l, m are integers with $l \geq 0$ and $|m| \leq l$. It can be shown (see, e.g. any text on spherical harmonics and [18, 19]) that l and m are related to the orbital angular momentum \mathbf{L} of the particle (about the center of the nucleus) with the magnitude of \mathbf{L} given by

$$L = [l(l+1)]^{\frac{1}{2}} \hbar \quad (2.24)$$

and its z -axis component

$$L_z = m_l \hbar. \quad (2.25)$$

The result is a shell arrangement that is similar to the atomic shell numbering, so that a similar shell labeling can be used. The energy levels are determined by the orbital angular momentum quantum number l using the s, p, d, f, ... letters to denote the values of $l = 0, 1, 2, 3, \dots$ respectively. The primary quantum number n does not have a physical meaning in the nuclear shell model nor does the value of n limit the allowed values of l as it does in the atomic shell model. This leads to the appearance of some shells such as 1f, 1g, etc. that are not seen in the atomic shell labeling.

The energy states of the bound nucleons can be calculated by solving the radial wave equation for a given orbital angular momentum l :

$$-\frac{\hbar^2}{2m} \frac{d^2 u}{dr^2} + \left[\frac{l(l+1)\hbar^2}{2mr^2} + V(r) \right] u = Eu. \quad (2.26)$$

Note that Eq. (2.26) uses the substitution $u(r) = rR(r)$ to simplify the form of the equation. Comparing Eq. (2.26) to the classical conservation of energy law with momentum p and potential energy V

$$\frac{p^2}{2m} + V = E \quad (2.27)$$

reveals that the bracketed portion of Eq. (2.26) represents the total potential energy of the nucleon. The interpretation is that the orbital angular momentum acts like an additional potential that adds to the central potential $V(r)$. Note that the angular momentum term, like the original potential field, is spherically symmetric, so solutions of Schrodinger's equation are still of the form of Eq. (2.21). The effect of the orbital angular momentum term in Eq. (2.26) is to move the wave function further away from the origin for increasing values of l . This influence can be seen by examining the bracketed expression in Eq. (2.26) for a finite potential well $V(r)$ function as shown in Figure 2.13. The orbital angular momentum represents an increase in potential energy over the negative potential energy of the finite spherical well, creating a potential barrier that is strongest near the center of the well ($r = 0$). Instead of a spherical well, the wave function is confined to a spherical shell when $l > 0$.

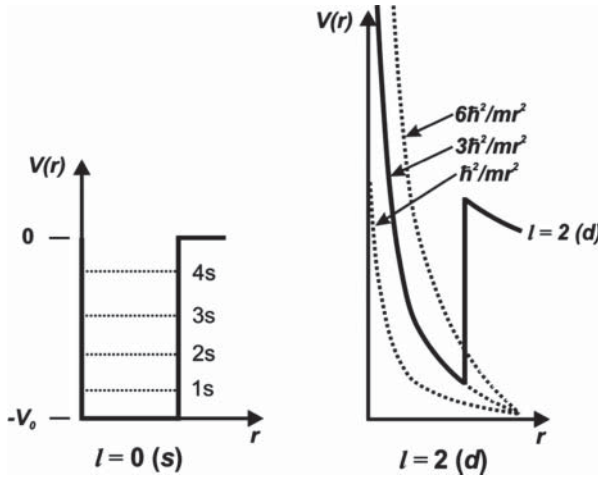


Figure 2.13 Superposition of the nuclear orbital angular energy in a finite spherical potential well. The $l=0$ state is shown at the left, with the energy levels indicated (not to scale). At the right is the $l=2$ state, but $l=1$ and $l=3$ orbital momentum components are also shown for reference.

Solutions to Schrodinger's equation are not easy to accomplish for most potential fields, but if the potential field is the harmonic oscillator potential:

$$V(r) = \frac{m\omega^2 r^2}{2} \quad (2.28)$$

closed forms for the energy states can be derived. No matter what potential $V(r)$ is used, the energy levels predicted by solutions of the radial function do not predict the shell closures for magic numbers above 20.

Around 1949, Maria Geoppert-Mayer, J. Hans D. Jensen, D. Haxel, and H. Suess independently realized that the nuclear potential is altered by the spin-orbit coupling of the nucleons. The nucleon orbital l and intrinsic spin $s = \pm 1/2$ angular momenta interact strongly so that the total angular momentum j is given by

$$j = l + \frac{1}{2} \text{ or } j = l - \frac{1}{2}. \quad (2.29)$$

This interaction can be modeled by adding a coupling term to Eq. (2.20):

$$V(r) = V_{ws}(r) + V_{so}(r)(L \cdot S) \quad (2.30)$$

that consists of a central potential $V_{so}(r)$ multiplied by the dot product of the orbital and spin angular momentum operators L and S , respectively. The new momentum operator J has the same correspondence to j as was used in Eq. (2.24) for the orbital momentum operator L and the quantum number l . Likewise, the same can be stated for the nucleon spin operator S and the quantum number s . The dot product in the coupling term further complicates the problem and destroys the spherical symmetry of the potential field. By noting that $J = S + L$ and also that

$$L \cdot S = (J^2 - S^2 - L^2)/2, \quad (2.31)$$

solutions to the radial equation can be expressed in terms $J(j)$ and $J_z(m_j)$. The J_z can be visualized as the addition of either the parallel or anti-parallel combinations of L_z

and S_z leading to Eq. (2.29). The spin-orbit interaction causes a spitting of energy states and becomes quite pronounced as the orbital angular momentum l increases. This effect causes a reordering of the shell energies so that the magic numbers above 20 are correctly predicted.

The shell model is useful for predicting nuclear spin and spin states, parity, and magnetic moments, but is better when applied to closed-shell or nearly closed-shell nuclei. The shell model, like the Fermi gas model, provides for a filling of states that is consistent with fermions. Momentum states are singly occupied and fill from lowest energy to highest energy. The total spin of the nucleus, denoted by I , can be determined because as nucleons are added to a nucleus, opposite spin states pair with each other to reduce energy. If it is assumed that the nucleons in closed shells do not contribute to the nuclear spin, the spin will be given by the nucleons that are outside closed shells. For this reason, even A nuclei will have an integer spin, whereas odd A nuclei will have a half-integer spin. For odd A nuclei, the spin is determined by the last nucleon that is odd. Nuclei with even Z and even N have a nuclear spin of zero. For odd Z and odd N nuclei, the last neutron couples to the last proton with their spins in parallel orientation.

Each of the nuclear energy states is labeled in a manner that is somewhat parallel to the labeling of the atomic energy states. The label indicates the orbital momentum state as well as the spin state, $l \pm \frac{1}{2}$. The spin state for the nucleus can be predicted. For example ^{16}O has magic numbers for both protons and neutrons and hence has a nuclear spin of zero; however, if a neutron is added, it will fill the next energy level, leaving ^{17}O with a spin of $5/2$ and a spin state of $(1d_{5/2})^1$. The parity of the spin state is found by examining the momentum state. The s , d , g , etc. momentum states are even parity, whereas the p , f , h , etc. momentum states are odd parity. For ^{17}O the momentum state is d or $L = 2$ and therefore is even parity. Taking a neutron away from ^{16}O to get ^{15}O results in odd parity, as the unpaired neutron is in a p state ($L = 1$).

While the shell model is predictive of observed nuclear behavior like shell closures, nuclear spin, and magnetic moments, the accuracy of the model is poor when the nucleus does not have closed or nearly closed shells. There are some aspects that are poorly modeled or missing altogether. Collective movement of nucleons is not modeled at all due to the starting assumption in the model for the treatment of nucleons as noninteracting point objects. Rotational and vibrational states as well as fission, particle capture, and emission cannot therefore be predicted.

There are also some isotopes that simply do not conform to the predicted shell behavior. For every element there is a point where no more neutrons can be added to the nucleus. In terms of Figure 2.12, the collection of these points is to the left of the stable isotopes and is called the neutron drip line. Some isotopes near the neutron drip line have very lightly bound neutrons that are not in the nucleus at all but occupy a halo around the nucleus. Examples of such halo nuclei include ^6He , ^8He , ^{11}Li , ^{11}Be , ^{14}Be , ^{17}B , ^{19}B , ^{19}C , and ^{22}C . One of the more scrutinized halo nuclei is ^{11}Li . First discovered in 1966, ^{11}Li was found to have a halo in 1985 by Isao Tanihata and his collaborators at Lawrence Berkeley Laboratory. It consists of a ^9Li core with a halo comprised of two neutrons. The seventh neutron in beryllium-11 surrounds the beryllium-10 core like a halo at a considerable distance from the core. Experiments on beryllium-12 indicate that the number of eight neutrons in beryllium isotopes is not a magic number [20]. In a like manner, there are isotones beyond which no more protons can be added to the nucleus. These can be represented by a proton drip line that is to the right of the stable isotopes in

Figure 2.12. There are some isotopes along the proton drip line that have lightly bound outer protons that form a halo around the nucleus. The known examples are ${}^8\text{B}$, ${}^{17}\text{Ne}$, ${}^{26}\text{P}$, and ${}^{27}\text{S}$. These exotic nuclei are the result of high-energy physics experiments and have very short lifetimes. They are detected in part because their cross sections indicate a nuclear size that is larger than predicted by formulas such as Eq. (2.4). While it might be tempting to think of halo nuclides as orbiting a core nucleus it is more realistic to consider them as low binding energy states near the top of the nuclear potential well with a halo that is caused by tunneling.

2.2.4.1.4 Other Nuclear Models The preceding discussion of the liquid drop, Fermi, and shell models for the nucleus provide the background for understanding various approaches to modeling the nucleus. As stated at the beginning of this section, nuclear models can be classified as central field or microscopic if they have weakly interacting nucleons. The shell model is an example of a central field model. On the other hand, the individual nucleons in the liquid drop model interact strongly with each other so this is an example of a collective or strong nuclear force model.

Independent Particle Model Ideally, the wave function for each nucleon in a nucleus could be calculated by taking into account all of the nucleon–nucleon interactions that are possible. Unfortunately, such an approach for n nucleons becomes increasingly complex, using either classical or quantum mechanics even for small values of n . Independent particle models assume the nucleons in the nucleus produce a stable field with a potential energy function. The shell model is an example or an independent particle model where the potential energy function is a relatively simple function. More advanced approaches approximate the n -body interaction of the nucleons with n single-body interactions. An initial trial potential energy function is used to solve for the nucleon wave functions and an iterative approach is used to refine the potential function to achieve a result closer to experimental observations. Like the shell model, this approach is not generally consistent with scattering experiments, which indicate a shorter nucleon mean free path than predicted.

Collective Model When a nuclear transition involves many or all of the nucleons acting together, the transition is called *collective*. Examples of collective transitions or movements in a nucleus include vibrations and rotations. The collective model was developed in 1953 by Aage Bohr and Benjamin Mottelson using prior work by James Rainwater. The model treats the surface of the nucleus like the liquid drop model with internal motions of the nucleons influencing the shape of the nucleus. The shape of the nucleus is not in all cases spherical, there are cases where the shape is an ellipsoid. Bohr and Mottelson found that the shape of nonspherical nuclei can be explained in terms of nuclear rotation. The collective model can be considered as an extension of the liquid drop model.

Cluster Model This model is also called the substructure model. It is based on the idea that certain combinations of nucleons produce stability. The pairing and asymmetry terms in the liquid drop model are examples of corrections due to nucleon clustering. In the former, like nucleons are energetically favored to form pairs, while in the latter, pairing between neutrons and protons is considered. The alpha (α) particle model is probably the best-known example of a cluster model appearing first as a type of liquid drop model

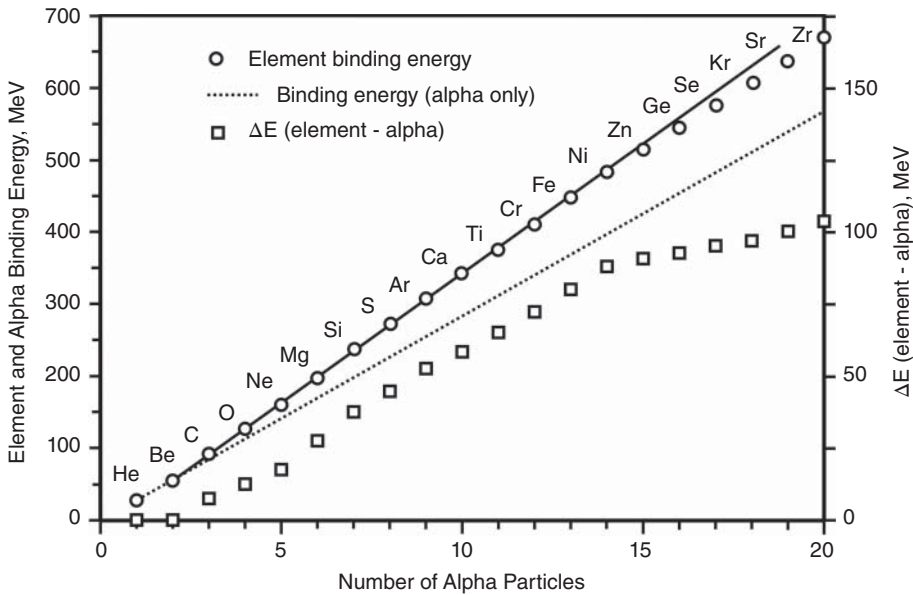


Figure 2.14 Binding energies of nuclei comprised of an integer number of alpha particles.

proposed by George Gamow in 1928 [4]. In this model, protons and neutrons when added to the nucleus will, whenever possible, form into alpha particle subunits. The compelling evidence for this model is alpha particle emission (Section 2.2.5.1) but a plot of the binding energies for nuclei comprised of an integer number of alpha particles, as shown in Figure 2.14, indicates a consistent binding energy for each additional alpha particle. The alpha particle model starts to fall apart when neutrons start to outnumber protons, so the model is best applied to low A nuclei.

Interacting Boson Model The interacting boson model (IBM) was created by A. Arima and F. Iachello [21] in 1974. In this model the protons and neutrons in the nucleus pair up and each pair acts like a single particle with the properties of a boson and angular momentum of 0, 2, or 4. While this model is based on the shell model, it reduces the complexity of the shell model by the combination of the nucleons in pairs, making the model attractive for describing nuclei with $A > 50$. The complexity of the shell model for nuclei in this atomic weight range limits its usefulness for predicting various nuclear states.

Lattice Model Lattice models try to reconcile the nuclear density of the liquid drop model with the shell structure of the shell model. They do this by exploring the properties of specific arrangements of nucleons or their constituent quarks in a given space or volume. This wasn't a popular direction for nuclear models until the 1960s following the discovery of quarks and neutron stars. Prior to this time, the lack of nuclear diffraction and the success of quantum mechanics and the uncertainty principle kept researchers away from investigating solid-phase nuclear models. The nucleon arrangements in lattice models resemble crystal lattices and are named accordingly. For example, there is a face-centered-cubic (FCC) arrangement proposed by Cook and Hayashi [22] and a

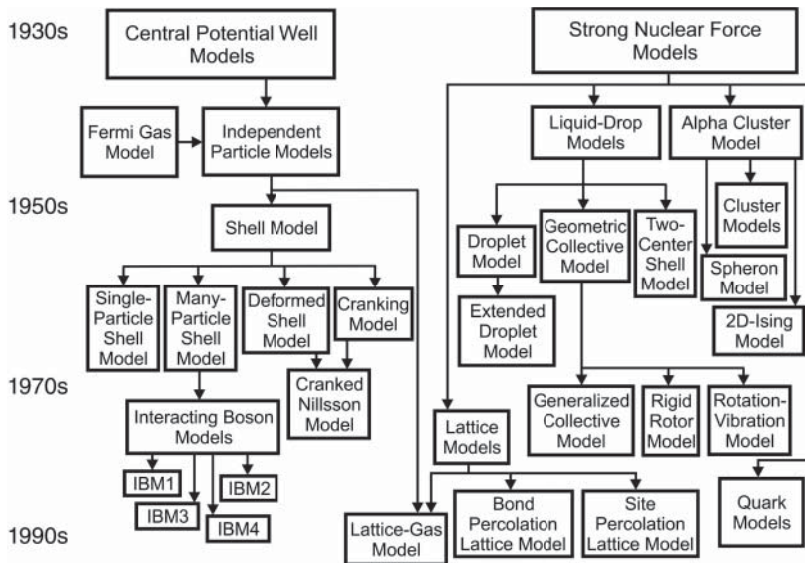


Figure 2.15 Evolution of nuclear models in the years since the 1930s. Source: Cook et al. 1999, Figure 1, p. 55. © 1999 IEEE. Reprinted, with permission, from [24].

body-centered-cubic (BCC) arrangement proposed by Nasser [23]. One of the hallmarks of lattice models is the massive amount of computation used to verify the models. For each arrangement of nucleons, a Monte Carlo approach is used to simulate the result of a neutron collision and the corresponding fragmentation of the nucleus. The results are compared to experiment to fine tune the nuclear structure.

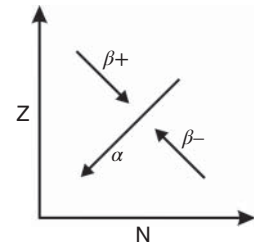
Lattice models provide answers to many of the observed nuclear properties. They provide a constant nuclear density like the liquid drop model but also offer insight for asymmetric fission. Lattice models have a shell structure because there is a relationship between lattice positions of nucleons and the quantum number in the shell model. Lattice models can also explain alpha particle emission.

The evolution of nuclear models in the years since the 1930s (Figure 2.15) provides a perspective for the effort extended to reconcile the good points about each classification of model with the observed behavior of nuclei.

2.2.5 Alpha and Beta Decay

An atom is said to decay when it changes into another element by emitting a particle or particles. Alpha and beta decay are two types of atomic decay that result in a transmutation of the original atom into another element. Alpha decay is a type of radioactive decay in which an atomic nucleus emits an alpha particle. The nucleus reduces both its neutron and proton count by two in this process. Beta decay consists of two complementary processes that allow an atom to obtain the optimal ratio of protons and neutrons. In beta decay, a proton is transformed into a neutron or a neutron is converted into a proton. The two types of decay are known as beta minus (β^-) and beta plus (β^+). Figure 2.16 illustrates the effect each of these decay processes will have on the neutron and proton

Figure 2.16 Illustration showing the effect that alpha and beta decay have on neutron and proton count in the nucleus.



count. Figure 2.16 can be compared to Figure 2.12, noting that beta decay brings unstable nuclei closer to the stable isotopes.

2.2.5.1 Alpha Decay

Alpha decay typically occurs only in heavy elements such as uranium, thorium, and radium. These elements have neutron-rich nuclei, which makes the emission of an alpha particle more likely. The process starts when several protons at the surface of the nucleus become somewhat separated from the rest of the nucleus. This can happen because of an imbalance between the short-range strong force and the longer-range repulsive Coulomb force between protons. Once there is sufficient separation, a more stable clump of nucleons, an alpha particle, is formed with enough energy that it can tunnel out of the nucleus. This process is shown schematically in Figure 2.17. The energies of two possible alpha states are shown. The higher-energy alpha state has a smaller barrier to tunneling and so has a higher probability of emission from the nucleus. It is also emitted with the same energy as its state while confined in the nucleus. This leads to a dependency of the emission probability on the emitted energy of the alpha particle, so that higher-energy alphas are emitted by isotopes with small decay lifetimes.

The relationship between alpha particle energy and the isotope decay constant is called the Geiger-Nuttall law and was first formulated by Hans Geiger and John Mitchel Nuttall

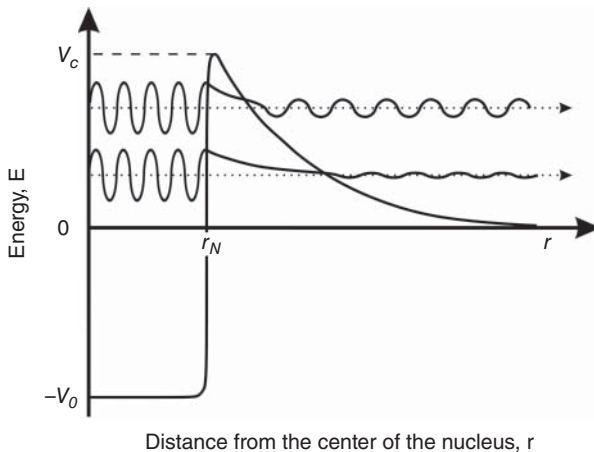


Figure 2.17 The emitted alpha particle energy is dependent on the emission probability (decay lifetime of the isotope).

[25]. Its modern form is

$$\ln \lambda = -a_1 \frac{Z}{\sqrt{E}} + a_2 \quad (2.32)$$

where λ is the decay constant, E is the total kinetic energy (alpha particle and recoil energy of the decaying isotope) and a_1 and a_2 are constants. The exponential relationship in Eq. (2.32) means a wide range in half-life results in a very narrow range in alpha particle kinetic energy. While this law was empirically derived in 1911 by Geiger and Nuttall, the theoretical cause due to tunneling was provided in 1928 by the Russian theoretical physicist George Gamov.

2.2.5.2 Beta Decay

Beta decay is a type of radioactive decay in which a beta particle (either an electron or a positron) is emitted from an atomic nucleus. This type of decay consists of two complementary processes, as indicated in Figure 2.16, that serve to move less-stable isotopes toward a more stable ratio of protons and neutrons. Both processes are mediated by the weak force, a force that seems to tear things apart rather than keep things together like the other forces. The weak interaction is responsible for the radioactive decay of subatomic particles and also plays an important role in nuclear fission. In β^- decay a neutron decays into a proton emitting an electron and an electron anti-neutrino. Likewise, in β^+ decay a proton decays into a neutron, emitting a positron and neutrino in the process. Both processes are best understood by an inspection of the Feynman diagrams for β decay in Figure 2.18. In β^- decay, the weak interaction converts a negatively charged $(-1/3e)$ down quark to a positively charged $(+2/3e)$ up quark with the emission of a W^- boson, which decays into an electron and an electron antineutrino.

It is worth noting that β^- decay is energetically favored because the mass of a neutron is greater than the mass of a proton. This means that an isolated neutron will always decay and has a half-life of about 10.5 minutes. Isolated protons and hydrogen nuclei, however, do not appear to decay and have a predicted lifetime of 10^{32} years or higher. In the nucleus, it is the change in binding energy that results in either β^- or β^+ decay. The emitted particles from β^- decay have a continuous energy spectrum, ranging from 0 to the maximal available energy. This spectrum is continuous because there is energy

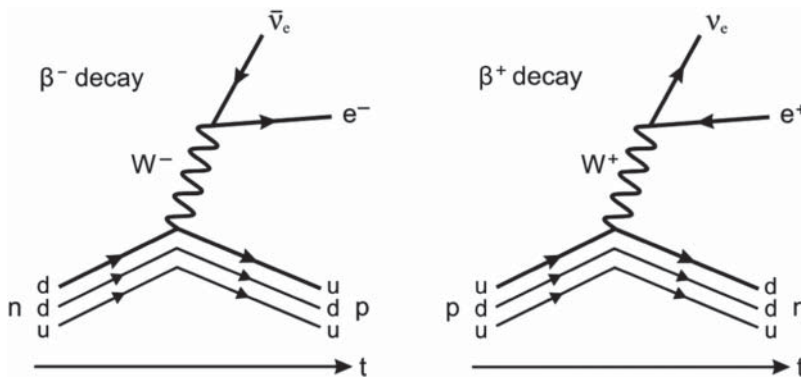
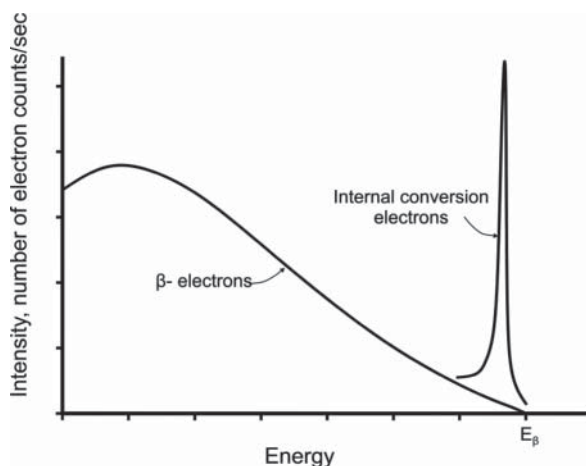


Figure 2.18 Feynman diagrams for β decay.

Figure 2.19 Typical energy spectrum for β^- decay. Internal conversion electrons are also shown.



sharing between the beta particle, the neutrino, and the rebound of the nucleus. Typical energies are around 1 MeV, but the range in energies can be from a few keV to 10 MeV or more so that the most energetic beta particles are ultra-relativistic.

There is a variation to the typical β^+ decay called electron capture. In a nucleus where β^+ decay is energetically allowed, the nucleus can capture an atomic electron emitting only a neutrino. This process is sometimes called K-capture, as it refers to the capture on an inner K-shell electron. There is also a process called bound-state β^- decay, which is only applicable for fully ionized atoms. In this process, the electron emitted during β^- decay is captured into a low-lying atomic bound state.

The typical beta decay energy spectrum indicated by the solid line shown in Figure 2.19 provides insight into the decay process. The difference in mass energies of the original neutron and the resultant proton, electron, and the electron antineutrino is distributed to the three particles as kinetic energy so the electron can have any energy up to the maximum available energy E_β . Another related process, internal conversion, is also shown in Figure 2.19. The kinetic energy imparted to the proton causes the nucleus to enter an excited state. This energy is usually released as a gamma ray photon (see below), but it can in some cases be imparted to orbital electrons with wave functions that overlap the volume of the nucleus. In this case, the energy of the electron is less than the energy of a gamma ray because the binding energy of the electron is subtracted from the available energy.

2.2.6 Gamma-Ray Emission or Gamma Decay

When a nucleus emits an alpha or beta particle, the nucleus can be left in an excited state. The emission of a gamma ray photon allows the nucleus to drop to a lower energy state (this is similar to the emission of photons by atomic electrons when they change to a lower energy state/orbit). The speed at which the gamma ray photon is emitted is on the order of 10^{-12} seconds, or nearly instantaneous with the alpha/beta decay emission.

A good example of beta decay followed by gamma photon emission is provided by Cobalt-60. Cobalt-60 is a radioactive isotope of cobalt that is produced artificially in nuclear reactors. It is often used for experimental purposes, including radiation testing of electronic parts. It has a half-life of about five years and decays into nickel-60

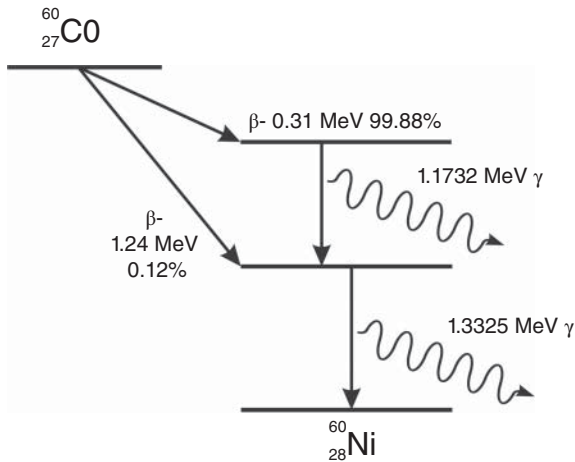


Figure 2.20 Energy diagram for Cobalt-60 β decay.

by β^- decay. A decay diagram for cobalt-60 (Figure 2.20) shows that most of the time, beta decay is followed by the emission of two gamma photons with energies of 1.17 and 1.33 MeV.

2.2.7 Other Types of Nuclear Radiation

Spontaneous fission is a type of radioactive decay where an atom's nucleus splits into two smaller nuclei and one to several extra neutrons. It is usually seen in atoms with atomic numbers above 90 and is a very slow process when compared to other types of decay. For example, uranium-238 decays by alpha decay with a half-life of about 10^9 years but decays by spontaneous fission with a half-life of 10^{16} years.

Proton emission and neutron emission can occur in a nucleus whenever there is an excess of protons or neutrons. In terms of nuclear stability, there are maximal extents to the proton/neutron ratio called drip lines. When a nuclide has too many protons or neutrons the excess particles can leak or drip from the nucleus until at least a somewhat stable nucleus can be established. Figure 2.21 illustrates a portion of a nuclide chart showing the decay process. Proton emission and neutron emission are the prominent processes at edges of the plot. The emission of a proton moves the nuclide down vertically in proton count toward a more stable nuclide. Likewise, the emission of a neutron moves the nuclide toward the left and to a more stable nuclide. Proton or neutron emission can be viewed more clearly in terms of the shell or the Fermi gas models for the nucleus. There simply are no more states available in the nucleus for a nucleon to occupy and no binding energy available. Protons that have a negative binding energy can tunnel through the Coulomb barrier and out of the nucleus similar to alpha decay.

Radioisotopes that decay predominantly by alpha emission can sometimes emit a fragment larger than an alpha particle in a process called *cluster decay*. As with alpha particle emission, the emitted particle or cluster tunnels through the nuclear Coulomb barrier. The emitted cluster is not quite large enough to be considered the result of fission.

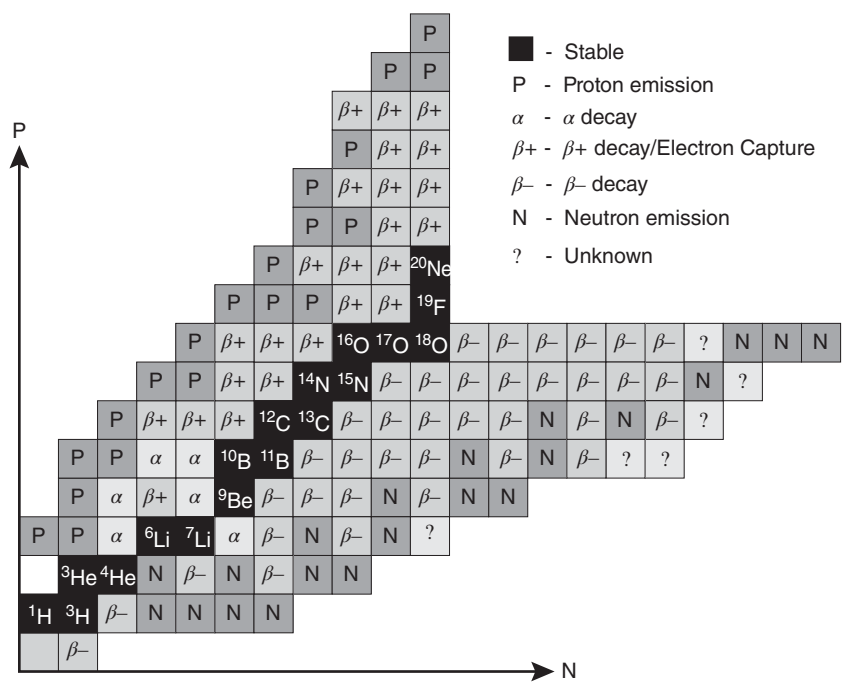


Figure 2.21 Portion of the nuclide chart showing decay mode. Source: Adapted from Chart of Nuclides, National Nuclear Data Center, <http://www.nndc.bnl.gov/chart>.

2.3 Natural Radioactivity

The discovery of natural radioactivity by Henri Becquerel a year after the discovery of X-rays led to a broader understanding of radioactivity and radioactive substances. It was Becquerel's experiments with radioactive elements and magnetic fields that helped to classify alpha, beta, and gamma radiation. The naming convention, however, can be attributed to Ernest Rutherford, who also discovered the differences in penetrating power between the three radiation types. Natural radioactivity has many uses today, including providing some of the best simulation sources for space and other total dose environments (Chapter 5). At the heart of natural radiation is nuclear decay, as discussed in the previous sections. The next few sections discuss how decay is measured and present the four decay series for the heavy radioactive elements.

2.3.1 Exponential Decay

Radioactive decay can be characterized in terms of exponential decay because the decay rate is proportional to the amount of material that has yet to decay. The relationship can be described mathematically by the first-order differential equation:

$$\frac{dN}{dt} = -\lambda N \quad (2.33)$$

with the solution

$$N(t) = N_0 e^{-\lambda t}. \quad (2.34)$$

The quantity N_0 is the original amount of material and λ is called the decay constant. The mean lifetime $\tau = 1/\lambda$ can be substituted in Eq. (2.34) and represents the average lifetime of an isotope before it decays. It is a simple exercise to derive the more familiar *half-life*, which represents the time it takes for a quantity of radioactive material to decay to half of its initial quantity. Often, there are several decay processes going on in the same sample of material. In this case, the decay constant can be treated as the summation of the various constituent decay constants. A more complicated situation arises when an isotope decays to another by one process and then into a third isotope by yet another process.

2.3.2 Decay Series

Elements with $Z > 83$ found in nature are radioactive (except for Bi 209, which is stable) and decay by alpha or beta emission until a stable isotope is achieved. The decay toward nuclear stability is usually the result of many intermediate beta or alpha decay steps. Noting that beta decay does not change the nucleon count in the nucleus, but that alpha decay decreases nucleon count by four leads to the possibility of four separate decay paths, which are illustrated in Figures 2.22–2.25. Three of these paths or decay series have long-lived isotopes at their starting points, so that these radioactive elements can still be found in nature. For example, the thorium series starts in nature with thorium 232 with a half-life of about 14 billion years. Likewise, the uranium and actinium series also begin in nature with the long-lived starting points of uranium 238 (half-life 4.4 billion years) and uranium 235 (704 million year half-life), respectively. The fourth decay

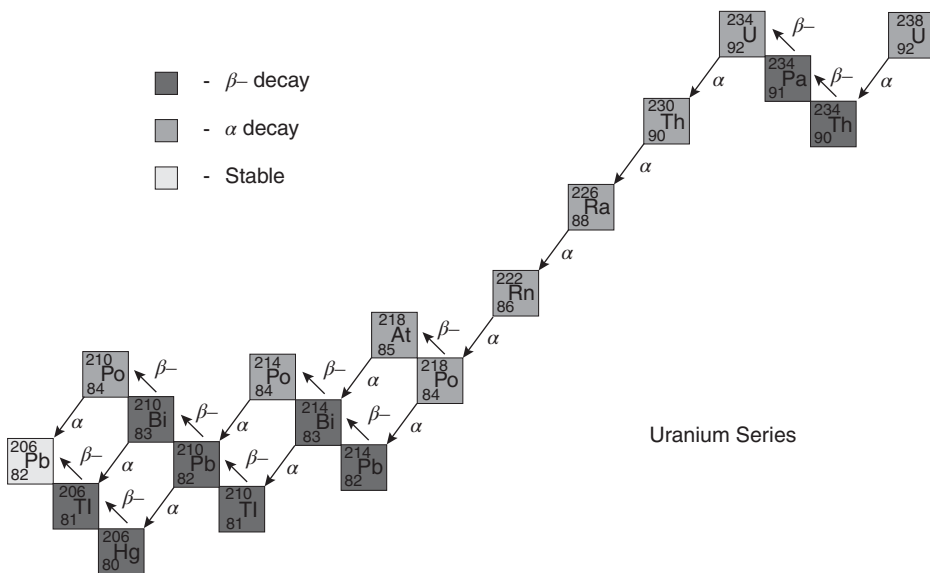


Figure 2.22 The uranium series.

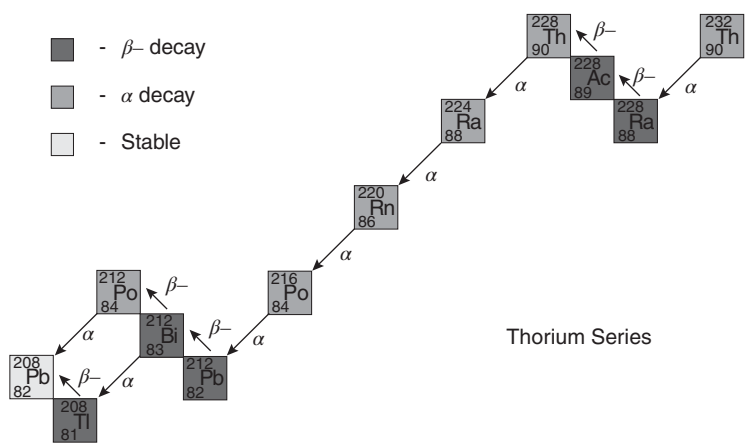


Figure 2.23 The thorium series.

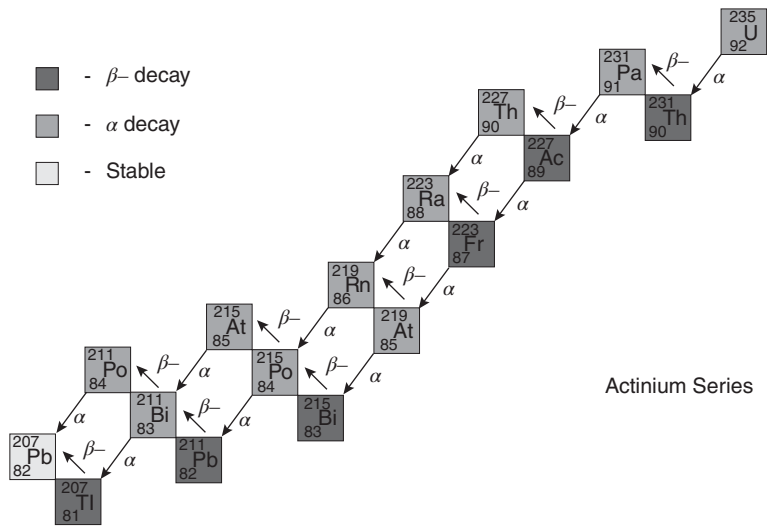


Figure 2.24 The actinium series.

series, the neptunium series, is comprised of mostly short half-life elements. Since the formation of the Earth products from this decay series have long since decayed away, leaving only the two last elements in the series, bismuth 209 and thallium 205, found in nature today.

Although Figures 2.22–2.25 are based on the natural starting points for each decay series, the decay chain for each series can be extended backward from the natural starting point to include elements not normally or easily found in nature. For example, americium 241 is used in smoke detectors and is normally produced by neutron irradiation of uranium or plutonium in nuclear reactors. It decays by alpha emission with a half-life of about 430 years to neptunium 237. The ending points for each decay series are also noteworthy. Stable elements at the end of the naturally occurring radioactive series all

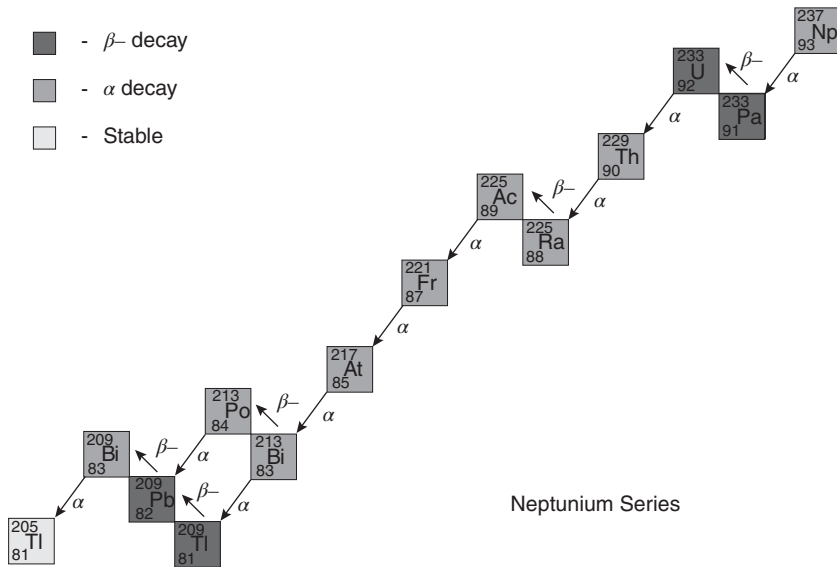


Figure 2.25 The neptunium series.

have magic number of neutrons or protons; the uranium series ends with stable $^{206}_{82}\text{Pb}$, the thorium series ends with $^{208}_{82}\text{Pb}$, and the actinium series ends with $^{207}_{82}\text{Pb}$.

A list of selected radionuclides and their properties is provided in Table 2.3. The list includes both naturally occurring and man-made isotopes and provides the decay energies from the most likely decay path. Medicinally important isotopes like ^{68}Ga , $^{99\text{m}}\text{Tc}$, and ^{103}Pd are made from precursor isotopes using specially made generators or cyclotrons while ^{60}Co , ^{238}Pu , ^{239}Pu , and ^{241}Am are the result of neutron irradiation. Naturally occurring ^3H and ^{14}C are the result of atmospheric neutrons (Section 2.4.4) interacting with nitrogen in the atmosphere



Nuclear reactors produce ^{239}Pu from neutron irradiation of ^{238}U and also ^{90}Sr and ^{137}Cs as fission products. Water-moderated reactors will also slowly build up ^3H , although ^2H has a very low cross section for neutrons.

2.4 The Space Environment

The radiation environment in space is highly complex and dynamic but can be roughly classified into solar radiation, trapped radiation, and cosmic rays. Solar radiation includes radiation and particle flux from the Sun, while trapped radiation includes radiation in the well-known van Allen radiation belts circling the Earth. Cosmic rays are actually high-energy particles that come from the Sun or from outside the solar system.

Table 2.3 Properties of naturally occurring and man-made radionuclides.

Nuclide	$T_{1/2}$	Decay process	Photon energy	Source	Usage
^3H	12.32 yr	β^- (18.6 keV)	—	NO, NR	Tracer for sewage and liquid wastes, nuclear weapons
^{14}C	5 730 yr	β^- (16 keV)	—	NO	Dating of carbon-containing items
^{36}Cl	3 01 000 yr	β^- (16 keV)	—	NO	Used to measure sources of chloride and the age of water
^{60}Co	5.3 yr	β^- (0.31 MeV) (1.48 MeV)	1.173 MeV 1.333 MeV	^{59}Co NI	Irradiation, sterilization
^{68}Ga	67.6 mo	β^+ (1899 keV)	—	^{68}Ge	PET and PET-CT imaging
^{90}Sr	28.6 yr	β^- (546 keV)	—	NR, NW	RTGs, industrial gauging
$^{99\text{m}}\text{Tc}$	6 h	γ emission	140.5 keV	^{99}Mo	Bone, tissue imaging
^{103}Pd	17 d	e- capture	21 keV	^{102}Pd , ^{103}Rn	Brachytherapy
^{133}Xe	5.3 d	β^- (346 keV)	81 keV	NR	Pulmonary studies
^{137}Cs	30.17 yr	β^- (512 keV)	661.7 keV	NR, NW	Irradiation, sterilization
^{210}Pb	22.2 yr	β^- (16.96 keV)	46.5 keV	NO	Sand, soil dating up to 80 yr
^{213}Bi	46 mo	α emission	440 keV	NR	Targeted alpha therapy (TAT)
^{235}U	703.8×10^6 yr	α emission	4.679 MeV	NO	Nuclear power and weapons
^{238}Pu	87.8 yr	α emission	5.593 MeV	^{237}Np NI	Pacemakers, RTGs
^{239}Pu	24 110 yr	α emission	5.245 MeV	^{238}U NI	Nuclear power and weapons
^{241}Am	232.2 yr	α emission	5.485 MeV	U, Pu NI	Smoke detectors

Key: NO, naturally occurring; NR, nuclear reactor; NI, neutron irradiation; NW, nuclear weapons.

2.4.1 Solar Radiation

The Sun is the dominant influence on the space environment within the solar system, with even energetic cosmic rays of extragalactic origin subject to the influence of the particles and magnetic fields of the solar wind. The Sun is an extremely active gaseous body at the center of the solar system, and both the particle and magnetic fluxes it emits are subject to large periodic and aperiodic variations. The 11-year solar activity cycle, for example, has been well known since first being identified in 1843 by the German

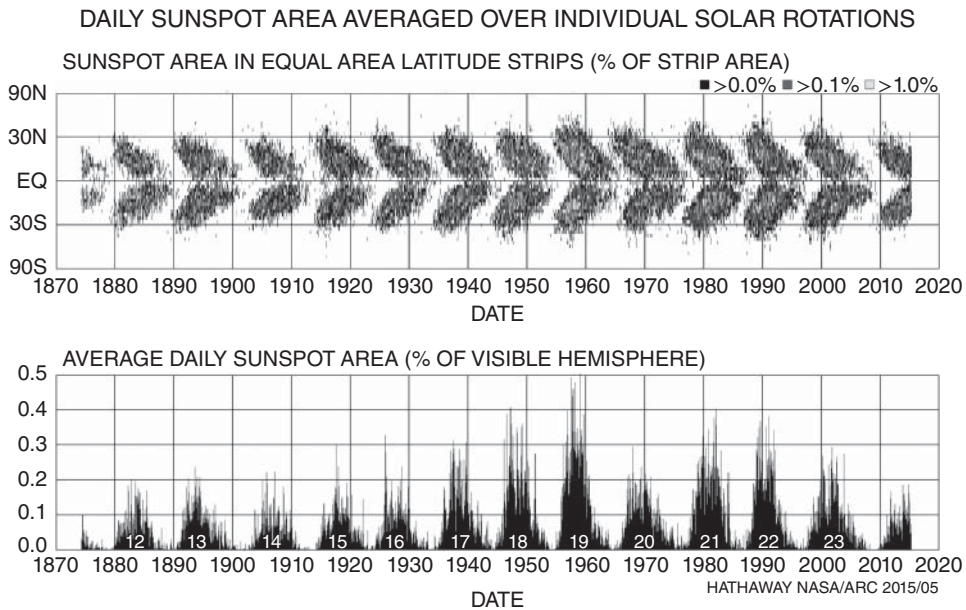


Figure 2.26 Daily sunspot area averaged over individual solar rotations. Source: <http://nasa.gov>.

astronomer Heinrich Schwabe. A plot of this cycle shown in Figure 2.26 covers sunspot observations over many years and provides sunspot size and latitudinal location (top plot) in what is sometimes called a *butterfly plot*.

The structure of the Sun includes several shells as indicated in Figure 2.27. The innermost core where nuclear fusion takes place is surrounded by a radiative shell, which is itself surrounded by a convection zone. The core is estimated have a radius of a quarter of the solar radius and a temperature higher than 15 million degrees Kelvin. The radiative shell is estimated to extend to about 70% of the solar radius and is about 5 million degrees Kelvin. Energy produced in the core is transferred primarily by radiation rather than convection in the radiative zone. Photons produced in the core can take over 150 000 years to reach the convection zone. The temperature in the convection zone is about 2 million degrees Kelvin. At this temperature the most efficient means of energy transfer is convection. The photosphere at the outer surface of the convection zone completes the visible areas of the Sun. It has a temperature between 4500 and 6000 K.

Two additional layers, the chromosphere and corona, are visible only during a total eclipse. The chromosphere is a low-density region about 2000 km deep above the photosphere but with a density of about 1/1000th that of the photosphere. The outermost layer of the Sun, the corona, extends out to several solar diameters and can be considered the rough equivalent of a planetary atmosphere. The corona is the origin of most of the solar particle and photon emission due to its very high temperature between 1–3 million degrees Kelvin and its extreme magnetic field intensities. In the corona, low mass particles such as electrons are accelerated to very high velocities sufficient to escape the Sun's gravitational field. The electron deficiency caused by the massive emission of negative charge results in intense localized charge imbalance conditions, creating high electric

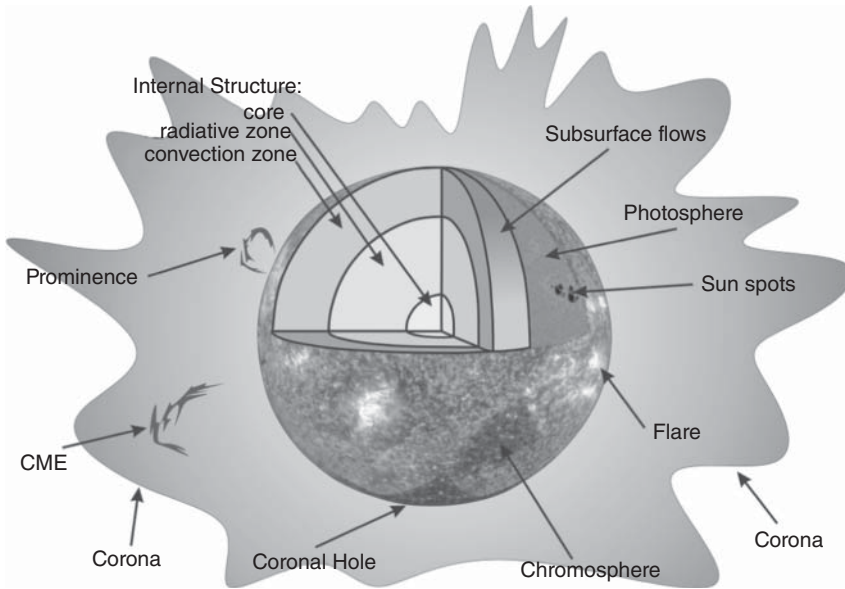


Figure 2.27 Diagram of the Sun. Source: <http://nasa.gov>.

fields, which, in turn, accelerate and eject other charged particles such as protons, alpha particles, and heavier ionized species.

The flow of electrons, protons, and other particles from the Sun is called the solar wind and extends into space well past the limits of the solar system, as shown in Figure 2.28. The influence of the Sun forms the heliosphere, an immense magnetic bubble, consisting of electrically neutral plasma moving away from the Sun at velocities ranging from 300 to 900 km/s and a temperature ranging from 1×10^4 to 1×10^6 K. The large volume of the heliosphere translates to a very low effective plasma density of 30 particles/cm³ within this volume, which is very nearly a vacuum. These conditions effectively define one of

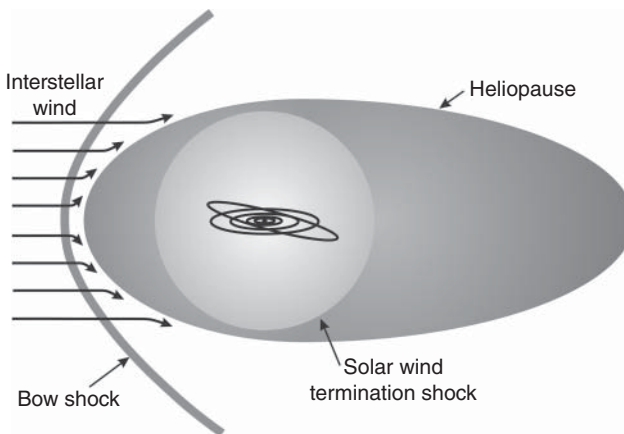


Figure 2.28 Diagram of the Sun's heliosphere and its interstellar interaction. Source: <http://nasa.gov>.

the basic properties of plasma. The solar wind consists largely of protons (95%), with positively charged He nuclei (alpha particles) and positively charged heavy ions making up the remaining 5%, and with enough electrons to provide charge neutrality within the overall system.

The boundary between the heliosphere and the interstellar medium is believed to be a structure somewhat similar to but much larger than the Earth's magnetosphere. This boundary is located some 10 billion kilometers from Earth, as estimated from *Voyager* data. It is dominated by the interaction of the interstellar medium with the solar wind, which creates a bow shock in the direction of the solar system's motion with respect to the rest of the local region of the Milky Way galaxy and an elongated tail in the opposite direction. An alternative to this classical interpretation is provided by recent *Cassini* mission data, which has suggested that the interaction between the solar wind and the interstellar medium is controlled by particle pressure and magnetic field energy density rather than by velocity with respect to the galactic environment, resulting in a more spherical region rather than the highly asymmetrical region predicted by classical theory.

The Sun displays other aperiodic phenomena, including the well-known solar flares as first described in 1859 [26], which are caused by the sudden release of magnetic energy stored in the solar corona. Flares appear as bright spots adjacent to sunspots, which are actually cooler regions, and affect all layers of the solar atmosphere. Solar flares release tremendous amounts of energy (to the order of 10^{25} J) over a broad range of the electromagnetic spectrum, ranging from gamma and X-ray radiation through visible light and radio frequency (RF) energy.

A solar flare will generally (but not always) trigger a coronal mass ejection (CME), which takes place in the chromosphere. CMEs consist of large volumes of plasma and entrapped magnetic fields, with a typical event ejecting some 10^{17} g (about 100 billion tons) of plasma into space. The plasma consists mostly of electrons and protons, but will also contain other species such as helium, oxygen, and some heavier elements. The correlation between solar flares and CMEs and the mechanisms behind CMEs are not yet well understood. It is believed that these phenomena originate as a result of disturbances in the coronal magnetic field, resulting in magnetic reconnection of opposing magnetic fields. This rearrangement results in a sudden release of energy stored in the magnetic fields, accelerating charged particles to relativistic velocities and causing the solar flare or CME. These solar phenomena occur more frequently in magnetically active regions of the Sun. The shock wave associated with CME events is responsible for large aperiodic increases in the solar wind velocity causing disturbances to the Earth's magnetosphere, including magnetic storms and radio interference. The analog of solar flares occurs on other stars, and these phenomena are known as stellar flares.

2.4.2 Trapped Radiation

As discussed briefly in Chapter 1, radiation belts surrounding the Earth were discovered in 1958 by James van Allen. The van Allen belts are comprised of electrons and protons that are trapped by Earth's magnetic field and are continuously fed and shaped by the solar wind. The cross section through the van Allen radiation belts was shown in Figure 1.5; Figure 2.29 more clearly indicates the relationship between the radiation belts and Earth's magnetic field. This magnetic field is a basic bipolar field ascribed to convection

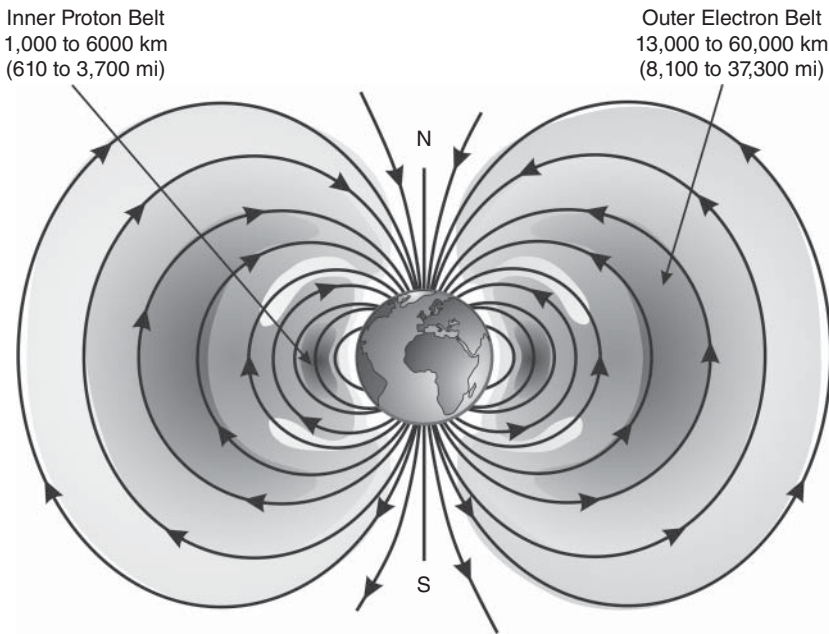


Figure 2.29 Cross-sectional view of the van Allen radiation belts showing their relationship to the Earth's magnetic field.

effects in the planet's metallic core, which is believed to be composed of liquid Ni-Fe. The magnitude and distribution of Earth's magnetic field are time variant, which results in periodic changes in the geographic location of the magnetic poles with respect to the rotational poles. The dipole component of Earth's magnetic field axis is not coincident with its rotational axis, but has an 11° offset [27, 28]. The magnetic North Pole is currently located at 76° North and 100° West and the magnetic South Pole is at 66° South and 139° East. The absolute value of the field in any fixed location also varies over a considerable range, from a few nanotesla (nT) at low latitude and high altitude to tens of thousands of nT at low altitude in the high-latitude polar regions. The field offset from the rotational axis also leads to variations in the altitude of the trapped radiation belts, mostly the inner (proton) belt, with the closest approach to the surface occurring in the South Atlantic Ocean off the South American coast. This is the well-known [29] South Atlantic Anomaly (SAA), which causes serious increases in proton and electron flux and which has historically resulted in persistent on-orbit system difficulties over this region. The SAA produces the majority of trapped radiation encountered in low Earth orbits (LEOs). Since these magnetic structures are at least somewhat symmetrical with respect to their axis (but not with respect to the Earth's axis), the corresponding Southeast Asia Anomaly on the opposite side of the Earth has the proton belt at a higher altitude, resulting in reduced trapped particle flux.

The majority of particles encountered in space and particularly in the near-Earth solar wind are electrons and protons. As these are both charged particles, they interact readily with electric and magnetic fields. The interaction between the solar wind plasma and the Earth's magnetic field distorts the field into a highly asymmetrical structure except

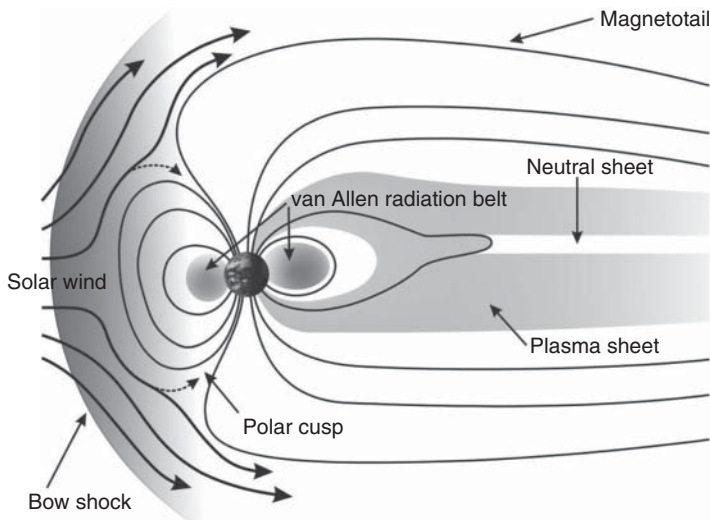


Figure 2.30 Structure of the Earth's magnetosphere under the influence of the solar wind. Source: <http://nasa.gov>.

in the near-Earth region of 4–5 Earth radii (R_e). Although not to scale, Figure 2.30 shows the distortion in the magnetosphere caused by the solar wind. The magnetosphere protects the Earth from the majority of solar wind particles and galactic cosmic rays; this geomagnetic shielding varies with latitude and is described quantitatively by the geomagnetic rigidity, which is defined as the resistance to charged particle deflection by the magnetic field. The magnetic rigidity of a charged particle is defined as its momentum per unit of particle charge, with the units working out to gigavolts (GV). The Earth's magnetic field offers the least protection at the poles, and the cosmic ray flux is the highest there. The cosmic ray flux ionizes air molecules in the upper atmosphere causing the Northern Lights or Aurora Borealis at the North Pole and the Southern Lights or Aurora Australis at the South Pole.

The solar wind plasma (mostly protons, with some heavy ions as well and electrons to achieve overall charge neutrality) and the magnetic fields embedded in the solar wind plasma interact with the magnetosphere and form it into a complex shape with several clearly defined regions. These regions include a hemispherical bow shock region facing the Sun with a radius of some 10–12 R_e (Earth radii) and a highly extended magnetotail facing away from the Sun; this region is roughly cylindrical with a diameter of approximately 40 R_e and can be as much as 300 R_e long. At the bow shock region, the solar wind is prevented from penetrating into Earth's atmosphere by the geomagnetic rigidity. This deflection mechanism results in the great majority of solar wind particles bypassing Earth entirely; estimates of the fraction of bypassed particles are as high as 99%. The bypassing mechanism also results in the stretching of the geomagnetic field into the magnetotail on the side of the Earth turned away from the solar wind. The ionosphere is the effective lower boundary of the magnetosphere, while the upper boundary is the interface between the magnetosphere and the solar wind plasma.

The magnetotail forms a first magnetic confinement system, in which solar wind particles are trapped; this region is called the neutral plasma sheet. A second trapping

mechanism is responsible for most near-Earth trapped radiation. These trapped particles consist mostly of electrons and protons with energies up to a few MeV, as higher energy particles such as cosmic rays will be deflected around the magnetosphere but not trapped. The trapping mechanism is interesting and involves the constraint of the charged particles by Earth's magnetic field lines through the Lorentz force, given by

$$d\mathbf{p}/dt = q\mathbf{v} \times \mathbf{B}. \quad (2.37)$$

in which \mathbf{p} is the particle momentum, q is the particle charge, \mathbf{v} is the particle velocity, and \mathbf{B} is the magnetic field intensity. The velocity is a vector quantity consisting of normal and parallel components to the magnetic field. The Lorentz force results in the charged particles oscillating (Figure 1.6) back and forth between the North and South Poles while performing a helical motion around the magnetic field lines and with a mirror point at each end of the trajectory. The period of this helicoid motion from pole to pole is to the order of a second for protons and perhaps 100 ms for electrons. Additionally, the magnetic field nonuniformity causes a slow precession of the particles, with the electrons drifting East and the protons drifting West. A complete azimuthal drift around Earth takes to the order of an hour, with a high degree of variability due to magnetic field disturbances. These multiple trapping and precessional effects result in clearly defined drift shells, or belts, of trapped (but not static; paradoxically, the particle needs to remain moving in order to remain trapped) particles. These charged particle belts were first discovered by James van Allen during the 1958 International Geophysical Year (IGY), and are appropriately known as the van Allen belts. The belts derive their long-term stability from four balancing phenomena: particle injection into the belt from the solar wind, particle acceleration due to the Lorentz force, particle diffusion, and particle loss. Short-term stability is driven by the solar wind's cyclic behavior superimposed on magnetic disturbances and solar rotation variations.

Not all planets have radiation belts. The minimum requirement for these belts to exist is driven by the minimum requirements for trapping charged particles; the planet's magnetic dipole moment must be sufficiently high in magnitude to stop the solar wind before it reaches the upper layers of the atmosphere, where deceleration will take place through collision (which is not a trapping mechanism) rather than through magnetic deflection. Within the solar system, Venus and Mars do not have magnetospheres and hence will not have trapped radiation belts, while Saturn, Uranus, and Neptune have magnetospheres but have weaker radiation belts. In contrast, the Jovian magnetic field is well over an order of magnitude more intense than that of Earth, which results in particularly intense Jovian belts that present particular challenges [30] for missions venturing into this environment.

Under normal conditions there will be two van Allen belts, the inner and outer. The inner belt consists of electrons and protons in the several hundred MeV energy range and extends from near the surface to approximately $2.4 R_e$. The outer belt extends from $2.8 R_e$ to $12 R_e$ and is composed mostly of energetic electrons up to 7 MeV energy, with some protons. The region between the belts is known as the slot. The belts vary in composition and altitude, and atmospheric disturbances such as magnetic storms or man-made phenomena such as high-altitude thermonuclear detonations have been known to greatly enhance the trapped particle flux in the belts and to even create a temporary third belt. A nuclear weapon detonation injects [31] energetic electrons from the beta decay of fission fragments into the near-Earth environment, and these

particles are trapped through the same mechanisms as solar electrons. This injected electron component is most stable and causes most damage at LEO altitudes.

The van Allen belts have been extensively mapped by satellites such as the Combined Release and Radiation Effects Satellite (CRRES), which gained insight into not only the belt environments but their effects on spacecraft electronics [32]. A mathematical description is a key requirement for modeling these regions for radiation environment prediction for different satellite orbits. Analytical solutions have not been found, as you would expect for such a large, varying and chaotic structure, and numerical solutions are the only practical approach. Modeling codes include AP8 [33] for protons and AE8 [34] for electrons, in which the “A” recognizes the leadership role of the Aerospace Corporation in first developing these models. AP8 was released in 1976 and was followed by AE8 in 1983. These codes are periodically updated, including the recent development [35] of the Monte Carlo Radiative Energy Deposition (MRED) code by researchers at Vanderbilt University. MRED introduced Monte Carlo simulation technology into this key set of tools. The codes develop predictions of trapped particle fluxes for any set of orbital parameters and mission duration. The solar cycle is modeled as a simple set of solar maximum and solar minimum values for the predicted fluxes. Figures 1.7 and 1.8 provided examples of AP8 proton flux maps. It becomes clear from this contour plot that the radiation profile will vary greatly depending on the orbit, with low Earth and geosynchronous orbits relatively benign and the highly eccentric Molniya orbits a much more difficult environment.

2.4.3 Cosmic Rays

The term *cosmic rays* has historical origins but is somewhat misleading, as these are not rays at all, but the term persists in the popular literature as well as in science. Cosmic “rays” are energetic charged particles originating in the Sun as well as outside the solar system; these are termed solar and galactic cosmic rays, respectively, and differ from other charged particles in that they are not trapped in the magnetosphere, usually due to their much higher kinetic energy. This high energy arises from the higher mass of the particles and from their sometimes extreme velocity, which can approach relativistic values. Cosmic rays are composed of 90% protons, 9% alpha particles, and 1% electrons, with some other particles such as heavy ions and neutrons as well. Solar flares emit large quantities of energetic charged particles, and this solar cosmic ray fluence is composed almost entirely of protons, with some alpha particles, heavy ions, and electrons. The magnitudes of these events vary, with the most active ones weakly correlated with the solar maximum part of the solar cycle.

Galactic cosmic rays originate outside the solar system, as the name implies. A background ionizing radiation component at the Earth’s surface was first described in the nineteenth century and was verified as originating beyond the Earth’s atmosphere through manned high altitude balloon experiments conducted by the Austrian scientist Victor Hess in 1912, using ionization chambers to detect the unknown radiation. Cosmic ray particles vary widely in energy, ranging from a few KeV for low-energy protons to relativistic heavy ions in the GeV range. A good reference plot of the cosmic ray flux as a function of energy is provided by Swordy [36]. In Figure 2.31 we show a log-log plot of galactic cosmic ray flux as a function of energy from the Particle Data Group (figure created by P. Boyle and D. Muller, source of data can be found in refs. 2

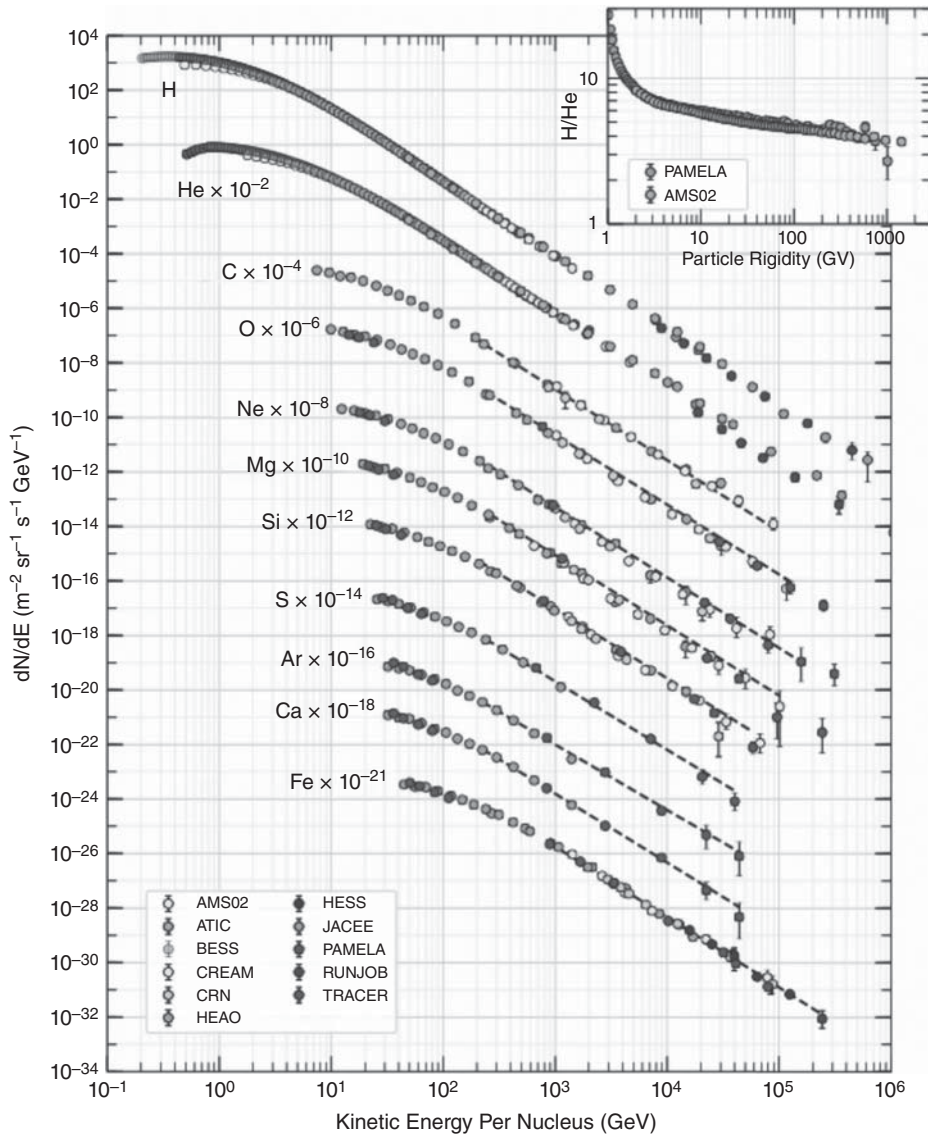


Figure 2.31 Galactic cosmic ray energy spectrum. Fluxes of nuclei of the primary cosmic radiation in particles per energy-per-nucleus are plotted vs energy-per-nucleus. Plot was created by P. Boyle and D. Muller, references for data can be found in [37]. Source: Tanabashi et al. (Particle Data Group) [37] 2018, figure 29.1.

through 13 in [37]). It is important to note that the tail of this distribution extends out to nearly arbitrarily high energies; the flux here is very low, but these few ions still cause fundamental difficulties in the cosmic ray hardening of satellite systems because of shielding ineffectiveness. Reasonable Al shielding thicknesses in the 100 mil (2.5 mm) range as commonly used in satellite airframes are effective at removing the low energy proton component, but have no effect at all on the high-energy end of the

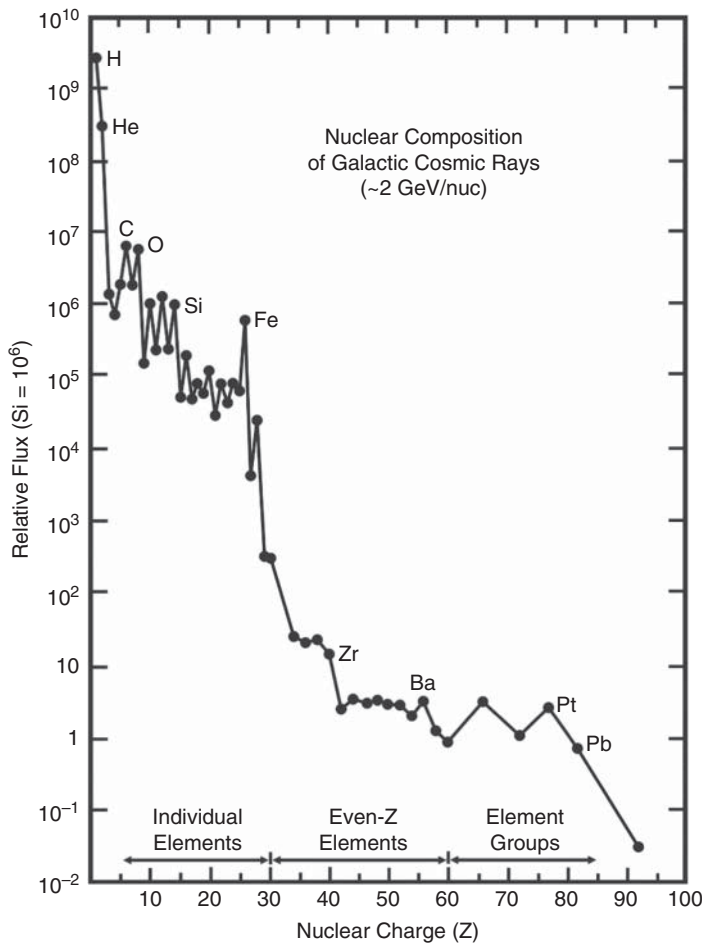


Figure 2.32 Galactic cosmic ray flux as a function of atomic mass, showing the dominant species below the Ni/Fe cutoff “knee.” Source: Mewaldt 1988 [38], Figure 1, p. 122.

distribution. Cosmic ray hardening must thus be carried out at the component level, through redundancy and error correction, as shielding is ineffective. The abundance distribution shown in Figure 2.32 plots the cosmic ray flux as a function of particle species [38] and has a similarly long tail, this time in the high atomic number species, which runs all the way to the transuranic elements and isotopes.

Characterizing cosmic rays requires very large detectors and long integration times to collect enough particles for even reasonable statistical significance, and the low flux at the higher-energy end of the spectrum makes this an inefficient procedure. As an example, the Heavy Nuclei Experiment (HEAO-3) was launched in 1979 to detect heavy and ultraheavy nuclei in cosmic radiation and consisted of two large argon-methane ionization chambers and Cerenkov counters read out by photomultipliers. HEAO-3 observed [39] over 100 high atomic number cosmic ray species between element 75 and element 87 in almost a year and a half of flight, and was much larger than most scientific instruments flown by NASA today. Much cosmic ray research today is performed on

Earth's surface using large arrays [40] of detectors, and a huge number of experiments are in progress. These can detect neutrons or charged particles through the light given off by the interaction between cosmic rays and gas molecules or liquid-based Cerenkov detectors. None of these arrays image incoming cosmic rays directly, but sense the secondary particle showers generated as the high energy particle interacts with the upper atmosphere. Most of the data agree with the theoretical upper limit to cosmic ray energy, the so-called Greisen-Zatsepin-Kuzmin (GZK) limit, caused by interaction of cosmic rays with the microwave background radiation. The highest energy cosmic rays appear to be of extragalactic origin but physicists puzzle over what process could produce such high energy particles.

In general, the origin of galactic cosmic rays is not well understood. The particle flux is isotropic, and as the charged particles are influenced by magnetic fields no clear point source can be determined. Low- to medium-energy cosmic rays with energies up to 10^{18} eV are believed to originate in the local Milky Way galaxy, with higher-energy particles of likely extragalactic origin. A number of theories have been advanced [41, 42], including an interpretation that galactic cosmic rays are accelerated in intense blast waves occurring as a side effect of supernova explosions and the interaction of supernova remnants with the interstellar medium. The remnants are expanding clouds of gas and magnetic field, and the violent interaction with their environment accelerates particles created in the supernova explosion. Particles are believed to oscillate within the magnetic fields, resulting in gradual acceleration up to the escape velocity, at which they escape the supernova remnant; this escape velocity depends on the volume of the acceleration region and the magnetic field strength. However, cosmic rays have been observed at much higher energies than can be theoretically predicted for supernova remnants to generate, and where these ultra-high energies come from is an active research topic. Leading theories include massive black holes at galactic centers, quasar activity, or the motion of galaxies through the intergalactic medium.

2.4.4 Atmospheric Neutrons

Atmospheric neutrons are a secondary effect of solar and galactic cosmic rays and arise from the interaction of galactic cosmic rays with the gaseous upper layers of the Earth's atmosphere, as discussed previously. The energetic cosmic ray particles collide with atomic nuclei and cause nuclear reactions, which result in a cascade of secondary particles including neutrons, protons, and pions. Recall that there is a small but nonzero flux of extremely high energy ions in the cosmic ray spectrum, and the interaction of these particles can lead to large cascades ("showers" of billions of secondary particles) of multiple energetic nuclear reactions. A diagram showing a portion of a cosmic ray shower or cascade is shown in Figure 2.33.

The incident particle in a cosmic ray shower or cascade shatters a nucleus in an air molecule, releasing numerous fragments, which go on to interact with other air molecules or decay in some way. The incident particle can also go on to interact with many more air molecule nuclei. The secondary particles from such interactions create various components of the cosmic ray cascade including electromagnetic, nucleonic/hadronic, and mesonic components. For example, π^0 mesons decay into two photons, which if energetic enough can produce one or more electron/positron pairs through pair production. Electrons and positrons can release photons through a

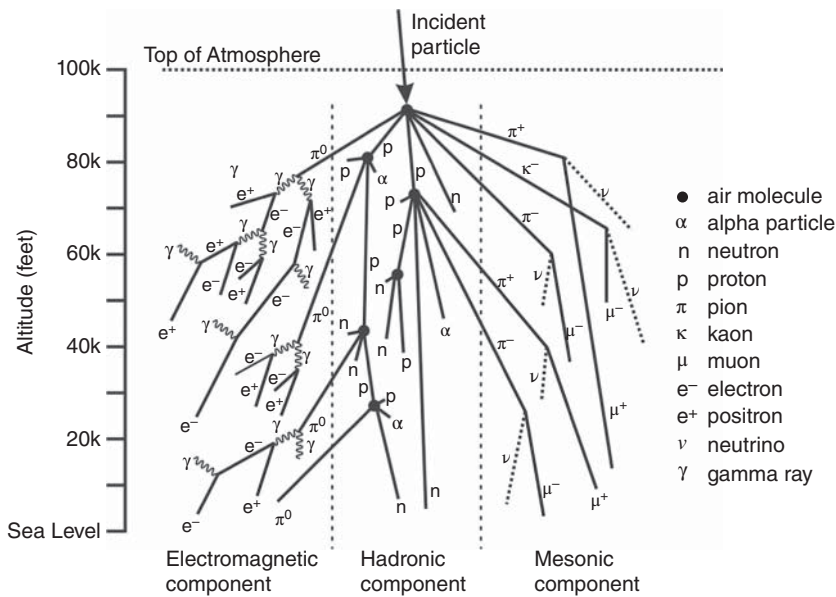


Figure 2.33 Diagram of a cosmic ray cascade.

process called bremsstrahlung, and bremsstrahlung photons can, if energetic enough, release energy to pair production. Such interactions comprise the electromagnetic component. The π^+ and π^- mesons contribute to the mesonic component and decay into muons and neutrinos. Muons can interact with nuclei or release bremsstrahlung photons if they have enough energy. The neutrinos are mostly noninteracting. Proton and neutron fragments, including alpha particles, can continue to interact with the atmosphere causing a continuance of the cascade until the energy imparted from the incident particle is dissipated.

Neutrons from cosmic ray cascades, called atmospheric neutrons, can have energies [42] ranging from 1 to 100 MeV, with the 1 MeV flux some three orders of magnitude higher than the 100 MeV flux. A plot of the atmospheric neutron flux as a function of altitude is shown in Figure 2.34. The maximum neutron flux of $1.2 \text{ n/cm}^2 \text{ s}$ is at 60 000 ft (20 km) and drops off by 60% at 30 000 ft and to 0.25% at sea level, at which there is still quite significant neutron flux. At commercial aircraft cruising altitude (10 km) the radiation is still several hundred times the ground-level intensity. Practical cosmic ray detection is carried out by detecting these nuclear reaction byproducts at the Earth's surface using detector arrays, as discussed previously.

Atmospheric neutrons are a relatively recent research topic but have been shown to cause a number of important effects, including primary radiation exposure to aircrew in high-altitude commercial aircraft. Neutrons represent about half the incurred dose in this environment, and significant research has been done in characterizing it; much early neutron mapping data was developed using the CREAM detector on transatlantic Concorde flights at up to 60 000 ft. These neutrons also cause single-event effects (SEEs) in electronics; since these are not charged particles, the mechanism is again one of nuclear reactions resulting in high energy ions and progressing to the ionizing effects of these ions, a process known as indirect ionization. A great deal of experimental work has

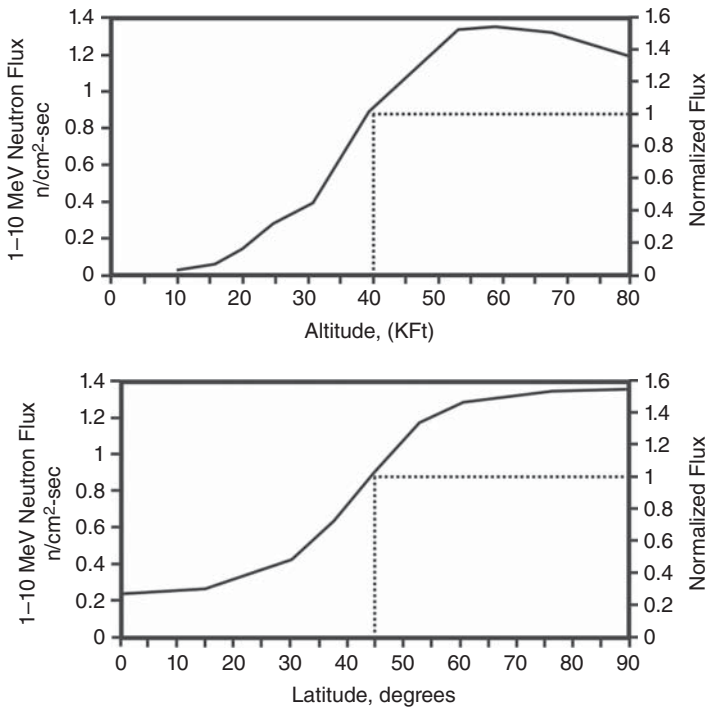


Figure 2.34 The atmospheric 1–10 MeV equivalent neutron flux as a function of altitude (top plot) and latitude (bottom plot). Source: Adapted from Taber and Normand 1995 [43], Figures 7-2 and 7-3, pp. 7-3 and Figure 7-4.

gone into characterizing high-altitude avionics systems for neutron SEEs [44], which is routinely addressed by hardware redundancy and error-correcting software. Upset rates of about 1 per 200 hours have been reported for the Boeing 777 autopilot system, which is orders of magnitude higher than the tolerances required by the manufacturers' requirements of 10^{-6} upsets per hour. Neutron SEE is also a threat in low-altitude atmospheric applications and is an important emerging threat in sea-level applications, such as server farms, and in high-density components such as a field-programmable gate arrays. In particular, for the higher-density processes such as deep submicron CMOS, the critical charge required for an upset is greatly reduced, and this makes the problem worse as the flux at lower neutron energies increases rapidly. Server farms can have 50 000 individual servers, and the statistics become very difficult as downtime in these installations is not well tolerated. Formally radiation-hardened components are not of much use here due to cost constraints, which dictate the use of commercial off-the-shelf (COTS) parts.

2.5 The Nuclear Reactor Environment

Nuclear reactors for commercial power generation present a much different but equally challenging and specialized environment. The reactor core itself presents too intense

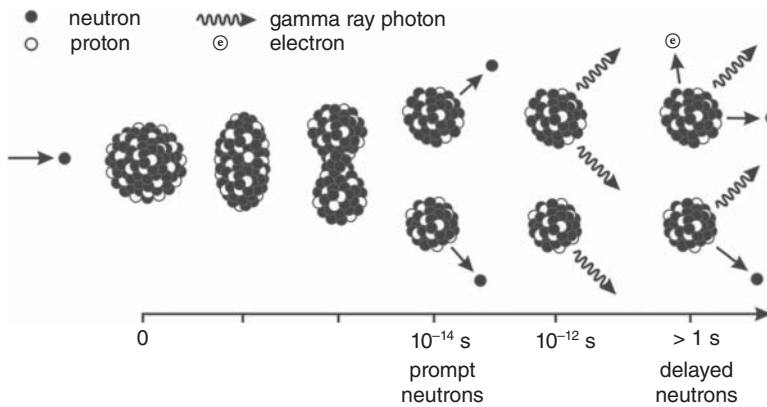


Figure 2.35 Fission reaction showing timescale and decay of the fission fragments.

an environment for the operation of nearly all practical electronic systems, but reactor safety, monitoring, and control systems are used outside the primary reactor shield. These environments are still orders of magnitude more intense than those encountered in space, with gamma radiation levels as high as 10 Mrad(Si) and 1 MeV equivalent neutron levels as high as 10^{15} n/cm². Much of the electronics for these applications use discrete semiconductors, with high-temperature wide bandgap materials, such as SiC and GaN provide an attractive solution.

Commercial nuclear power installations are built around a reactor core using, for example, ²³⁵U or ²³⁹Pu fission material to sustain a continuous but controlled nuclear reaction [45]. This process is based on neutron-induced fission of the fuel material as indicated in Figure 2.35. This figure provides a time-based diagram of the fission event as well as decay that happens in the fission fragments. A neutron hitting the nucleus causes it to enter a vibrational mode that is reminiscent of those from the liquid drop model. After several femto-seconds, the nucleus splits approximately in two and releases a few free neutrons as well. The free neutrons, coming from the initial fission event, are called prompt neutrons. As the fission fragments settle, they emit gamma ray photons. Many fragments are short-lived and undergo beta decay and/or emit neutrons to achieve stability. Neutrons emitted by fragments are called delayed neutrons and occur about a second or longer after the original fission event.

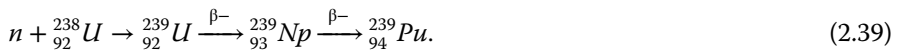
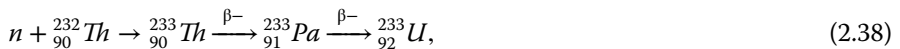
In a nuclear chain reaction, prompt and delayed neutrons contribute to further fission reactions, which lead to more neutrons feeding the reaction. A chain reaction is said to be critical if every fission event produces a neutron that also causes fission. If a reaction is critical due to the contribution of prompt neutrons alone any additional neutron production would quickly take the reaction out of control. This is due to the prompt nature of these neutrons – no control loop can react quickly enough to their production. In practice, nuclear reactions in power stations are kept subcritical with respect to prompt neutrons with the control loop geared toward the criticality of the delayed neutrons. Neutron absorption in control rods and reactor coolant are used to control the degree of criticality of the reaction, avoiding the uncontrolled chain reaction on which nuclear weapons are based. The control rods are composed of materials of a high neutron capture cross-section that efficiently absorb neutrons without themselves

Table 2.4 Comparison of the fission critical energy to the neutron binding energy for various isotopes used in nuclear reactors.

Nucleus	Critical energy (Mev)	Binding energy of last neutron (Mev)
^{239}Pu	5.0	6.6
^{238}U	7.0	5.5
^{235}U	6.5	6.8
^{233}U	6.0	7.0
^{232}Th	7.5	5.4

becoming unstable; typical materials include AgInCd alloys and B-based alloys. The physical position of the control rods within the core determines the amount of neutrons absorbed and hence the power output of the reactor. In case of emergency, the rods can be rapidly dropped into the core to immediately reduce criticality and stop the chain reaction. The fission of the ^{235}U or ^{238}Pu atoms releases neutrons, heat and gamma rays, and the absorption of neutrons reduces their energy in a process known as thermalization. The intense neutron environment activates other materials rendering them radioactive as well. These activated materials also produce further energy by decay of unstable isotopes.

Very few radioactive isotopes can be used as fuel in a nuclear reactor. The viable candidates are listed in Table 2.4 along with critical energies needed for fission and binding energies for the last neutron in each nucleus. For ^{233}U , ^{235}U , and ^{239}Pu , the critical energies are lower than the binding energy for another neutron. This means that these nuclei are fissile or easily fissionable, even with very slow neutrons. On the other hand, ^{238}U and ^{232}Th will likely absorb a slow neutron, with fission occurring only in ^{238}U if the neutron can provide the energy difference between the critical energy and the neutron binding energy. While ^{238}U nuclei are fissionable with fast neutrons, a chain reaction cannot be sustained because of inelastic scattering of fast neutrons to below the critical energy. However, both ^{238}U and ^{232}Th are fertile – they can be converted into fissile nuclei by absorbing neutrons in a breeder reactor:



The fission of ^{235}U releases a large amount of energy – around 200 MeV. This energy is shared by the fission products and fission neutrons. Fission neutrons are thus very energetic and are called fast neutrons because most of them have energy greater than 1 MeV. An energy spectrum for prompt neutrons from ^{235}U fission is shown in Figure 2.36. The neutron energy in this spectrum, sometimes called a Watt distribution, is a calculated spectrum by David Madland [46] under the assumption of first-chance fission only that shows the dependence of the spectrum on the kinetic energy of the incident neutron.

The Watt distributions as in Figure 2.36 can be described by the empirical probability function:

$$P(E) = 0.4865 \sinh(\sqrt{2E})e^{-E} \text{ MeV}^{-1}. \quad (2.40)$$

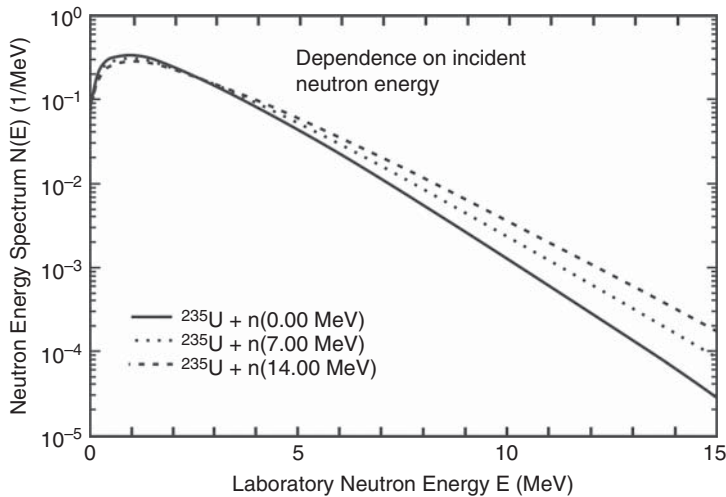


Figure 2.36 Dependence of the prompt fission neutron spectrum on the kinetic energy of the incident neutron, for the fission of ^{235}U . Source: Madland 1982 [46], Figure 2, p. 5.

While it is not obvious due to the linear energy scale of Figure 2.36, Eq. (2.40) indicates that very few prompt neutrons have energy in the thermal range (a few eV) that is favorable for fission of ^{235}U . For this reason, nuclear reactors utilize materials that moderate the energy of neutrons to increase the number of thermal neutrons. Moderating materials include water, heavy water, and carbon as these materials slow down neutrons through inelastic collisions providing more neutrons for fission.

The prediction from the liquid drop model for equally sized fission fragments is not born out in nature. Fission of ^{235}U by thermal neutrons usually results in two fragments of unequal size centered at $A = 95$ and $A = 137$ along with several fission neutrons. These fragments, in turn, decay, usually through beta decay, to more stable elements.

The reactor core thus releases large amounts of energy through various nuclear reactions; as mass and energy are related by the well-known Einstein equation, nuclear reactions are a great deal more energy-intensive than chemical reactions and nuclear materials have the highest energy density of any fuel. One kilogram of ^{235}U processed through a nuclear reactor will yield 7.2×10^{13} J, while burning the same quantity of coal releases 2.4×10^7 J, which is a six order of magnitude difference. These large amounts of thermal energy are removed from the core by a primary cooling loop, using either water or, alternatively, molten metals or salts, transferring the energy as well as preventing the core from melting down. This entire loop is highly radioactive and it, the core, and peripheral equipment are enclosed in a concrete and steel containment structure. The heated coolant is circulated through another heat exchanger, transferring the energy to a secondary water loop that is not radioactive and that is then used to drive turbines with superheated steam. The radiation environment within the containment facility consists of neutrons, gamma radiation released by nuclear reactions between neutrons and the surrounding materials, and (under accident conditions) protons and electrons. Table 2.5 summarizes the representative radiation environments found in a nuclear power plant. Unlike the weapons environment, there are no transient effects to be considered in reactor applications, as the dose rates are moderate. Compared to

Table 2.5 Representative radiation environments in a nuclear power plant. Both the normal and loss of coolant accident (LOCA) levels are shown.

Environment	40-year normal operation level	Peak level, accident	Units
Neutrons, 100 KeV, dose	1×10^9 to 1×10^{14}	—	n/cm ²
Neutrons, 100 KeV, dose rate	1×10^1 to 1×10^5	—	n/cm ² s
Gamma, dose	1×10^3 to 1×10^8	1×10^7	rad(Si)
Gamma, dose rate	1×10^{-3} to 1×10^2	1×10^6	rad(Si)/h
Electrons and protons	—	1×10^8	rad(Si)

Source: Adapted from Johnson et al. 1983 [47], table 2, p. 4359.

space applications, the levels encountered are very high, although the dose rates and operational times are somewhat comparable.

Hardening of nuclear power plant electronics is accomplished by using critical control functions designed as simply as possible and by using a combination of shielding and radiation-hardened parts. Hardened parts for this environment present a serious procurement and obsolescence problem, as sources and parts selection are very limited. Shielding is an attractive method and widely used, as the stringent weight considerations found in space and mobile applications are of no immediate concern in reactor applications. Hardness requirements are also heavily driven by accessibility, as the electronic systems in the containment structure cannot be directly serviced on a routine basis. Much of the work within these structures involves the handling of highly radioactive materials, which necessarily needs to be carried out by robots, and mobility requirements for these machines are stringent and use multiplexed control signals rather than direct heavy cable bundles.

2.6 The Weapons Environment

Weapons spectra were part of the very earliest studies of radiation effects in electronics. These environments are driven by the detonation of nuclear weapons of both the fission and fusion type, which we euphemistically called devices in the Cold War years. In Chapter 1, we discussed the very limited experience with which the nuclear powers undertook their testing programs, driven by the pressures of war, and the long learning curve that eventually enabled engineers to understand the effects of the various types of radiation on electronics. Weapons spectra are in nearly all cases much different from the space environments we're now familiar with and are largely classified, and will be discussed only in general terms.

A fission weapon uses a nuclear reaction in which heavy atoms such as ²³⁵U or ²³⁹Pu are split into lighter species, releasing the mass differential as energy as discussed above. In these weapons, two subcritical masses of fissionable material are driven together by external means or a single subcritical mass is compressed into a single supercritical mass, which then initiates an uncontrolled chain reaction and explodes (Figure 2.37). Early fission weapons used a simple gun-type arrangement to drive the two masses together, while later devices used an implosion driven by precisely machined shaped



Figure 2.37 The Crossroads Baker nuclear event at Bikini Atoll. This was a 23 kt device exploded as part of Operation Crossroads, which investigated the effects of fission weapons on naval assets; note the silhouettes of ships near the event site. Source: US DoD.

charges. In contrast, a fusion or thermonuclear device uses a similarly uncontrolled reaction between light isotopes of hydrogen, which combine into helium accompanied by the release of large amounts of energy. A practical fusion weapon uses a fission device as a primary source of energy to drive the fusion reaction of hydrogen isotopes, a nuclear reaction that is entirely similar to those driving the processes in the Sun. Both classes of devices result in large amounts of released energy, which consists of blast (shock waves), thermal radiation, ionizing radiation, and neutrons. Our interest is in the ionizing and neutron components of the released energy.

Figure 2.38 provides the time dependence of gamma ray output from a hypothetical nuclear explosion [48]. Gamma radiation is produced directly by the nuclear reactions that constitute the explosion, and indirectly by interaction of prompt neutrons with the atmosphere and the decay of residual nuclear reaction products, which include fission debris and radioactivity in materials as induced by neutron activation. The explosion emits products in a definite sequence, starting with a short (about 20–100 ns) burst of gamma rays and neutrons occurring before the device has fully disintegrated. The intensity of these emissions depends very heavily on the type of weapon and the specific design and burn rate. This process is followed by a burst of fast neutrons, which are very penetrating and are not absorbed.

A fusion weapon will produce more neutrons per kiloton of yield, and these neutrons are generally more energetic than fission neutrons; a fission weapon can thus be optimized for maximum neutron yield and minimum blast, minimizing physical damage and maximizing lethality. The fast neutron burst is also a source of secondary gamma radiation through energy loss and activation, as the neutrons are absorbed by the atmosphere. The time constant for this process is to the order of microseconds. A thermonuclear detonation neutron energy spectrum [49] has many of the same properties as the Watt distribution for fission of ^{235}U . There is a peak flux around

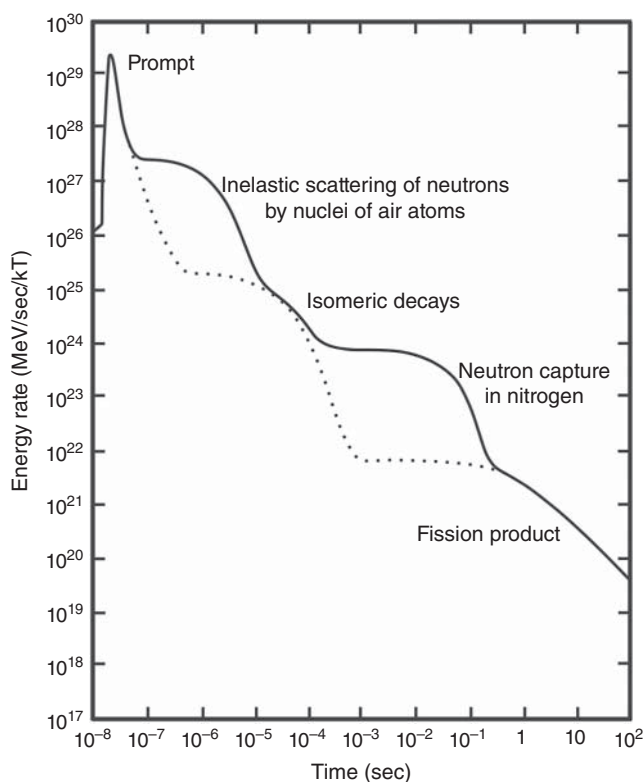


Figure 2.38 Calculated time dependence of the gamma ray energy output per kiloton energy yield from a hypothetical nuclear explosion. The dashed line refers to an explosion at very high altitude. Source: Glasstone and Dolan 1977 [48], Figure 8.14, p. 328.

0.8 MeV for fission produced neutrons with an average energy of about 2.0 MeV. There is also a peak at 14 MeV that is associated with fusion-produced neutrons.

The neutron fluence from a nuclear explosion can be estimated from the empirical equation [50]

$$\Phi_n = \frac{2 \cdot 10^{25} Y}{r^2} e^{-(\rho r / 2.38 \cdot 10^4)} \text{ n/cm}^2 \quad (2.41)$$

where Y is the yield of the detonation in megatons, r is the distance from the detonation in cm, and ρ is the density of the air in grams per liter ($\rho = 1.1$ for sea-level air). Equation (2.41) includes an attenuation by $1/r^2$ due to the geometry of the explosion and an exponential term to take into account the atmospheric attenuation.

The explosion also generates substantial amounts of fission products with very short half-lives (milliseconds to minutes), including the remnants of the bomb's structure. The rapid decay of these isotopes generates debris gamma radiation but is essentially complete within 10 seconds. The relative proportion of these gamma ray and neutron sources depends on the device yield. Tactical devices with yields to the order of a few kilotons can generate up to 25% of the gamma dose from direct gamma and neutron reactions,

while this contribution is essentially zero for larger thermonuclear explosions. References on these weapons environments are expectedly uncommon in the open literature, but health physics journals are a resource. For a discussion of the physics of weapons effects on electronics the very early Nuclear and Space Radiation Effects Conference (NSREC) Short Course notes (1980, 1982, and 1984) provide [51–53] a reasonable background.

Survivable electronic systems in the nuclear weapon environment present an entirely different set of challenges than space or reactor applications. The key difference is the dose rates involved. Gamma radiation dose rates in space are generally low, as we've seen, to the order of a few millirad(Si)/s with important exceptions in such places as the Jovian radiation belts. Industrial acceptance testing of hardened parts is commonly performed within the 50–300 rad(Si)/s, a few orders of magnitude above that. A nuclear event however has dose rates in the 10^9 – 10^{11} rad(Si)/s range, with 20–100 ns pulse widths. The time integral of the pulse is the total dose, which can run in the hundreds of kilorads even for these short pulse widths. The high dose rate drives a correspondingly high rate of electron–hole pair generation, which reduces the semiconductor material resistivity to a very low value, and also generates high photocurrents (amperes) in p–n junctions. These effects usually latch the device or result in a low-resistance path between the supplies. In the absence of protective measures, the part will be destroyed through excessive current leading to damage to interconnect metallization and bond wires. Protection can be implemented at the system level through a nuclear event detector, which is a PIN diode-based transient gamma detector that generates a signal used to crowbar the power supplies of critical functions. Protection can also be done at the part level, using a combination of on-chip current limiting resistors, photocurrent compensation diodes, and nonlatching dielectrically isolated processes, and this has been the historical approach in US strategic systems.

It should also be noted that neutron levels in nuclear weapons environments are correspondingly high, with fluences as high as 1×10^{15} n/cm². This leads to displacement damage effects in which one or more silicon atoms are displaced from the lattice, creating a Frenkel pair. This model is simplistic, as the actual process involves a great many lattice sites and results in a defect cluster [54]. The lattice damage results in reduced minority carrier lifetime, with actual resistivity shift (in the direction of increased resistivity) occurring at very high levels. This radiation damage affects mostly bipolar junction transistors, which are a minority carrier device, with less of an effect on MOSFET devices. Hardening is accomplished through higher doping levels, narrower base width, and shallow junctions, and as a general rule higher F_T devices will be harder in the neutron environment. All parts hardened to weapons environments are highly application specific and closely export controlled, and the use of commercial components in strategically hardened systems is uncommon.

2.7 The Environment in High-Energy Physics Facilities

This is another interesting man-made environment that is specific to the large particle accelerator facilities used for the experimental aspects of high-energy particle physics. The leading accelerator facility in the current high-energy field and the one defining the state of the art in this field is the Large Hadron Collider (LHC) at the Conseil Européen

pour la Recherche Nucléaire (CERN) facility, located on both sides of the French-Swiss border outside Geneva, Switzerland. The facility and experiments have a number of physics objectives including confirming the existence of the Higgs boson and alternative symmetry-breaking mechanisms and the exploration of alternatives to the standard model of particle physics. LHC is located in a 27 km circumference tunnel, which is reused from the Large Electron-Positron Collider (LEP) project and accelerates two counter-rotating proton beams to a peak energy of 7 TeV, resulting in highly energetic proton–proton collisions. In order to create a sufficient number of collisions, LHC is capable of reaching an unprecedented peak luminosity of $10^{34}/\text{cm}^2 \text{ s}$ at two high luminosity interaction points. At this peak luminosity, LHC will produce nearly 1×10^9 p–p collisions per second, creating an extremely hostile radiation environment near the beam line, the deflection magnets, and at the experiments. These are the most intense radiation fields found in any large-scale particle physics experiment and require specifically radiation-hardened design and hardware for the control electronics and the experiments.

An experiment in this context is a very large (perhaps 20 m in diameter) vertex detector consisting of a number of cylindrical detector arrays of several types, all coaxially surrounding the beam interaction region and operating in an externally applied magnetic field of to the order of 3T. The collision products are tracked by the detectors, and the resulting signals are routed into massive data acquisition systems of tens of millions of channels each. Since the particles are charged, the mass and momentum can be derived from track curvature and magnetic field strength. The resulting amount of data is massive, and a substantial amount of real-time data filtering is performed that allows only “interesting events” to be further processed and discards most others. Even with data filtering the amount of data generated by LHC is enormous, adding up to some 15 PB per year (15 million gigabytes or nearly 2 million dual-layer DVDs). The data is processed by a distributed computing network operating in 34 countries, not a surprising approach from the organization that pioneered the World Wide Web as a means of scientific communication. After initial processing, the data are distributed to 11 primary computer centers in Canada, France, Germany, Italy, the Netherlands, Scandinavia, Spain, Taiwan, the United Kingdom, and the United States. These primary centers then distribute the data to some 160 secondary centers for analysis. A backup of all data is retained on tape at CERN.

There are seven principal experiments at LHC, including the “Compact Muon Solenoid” (CMS), the “Toroidal LHC Apparatus” (ATLAS) and the “Large Ion Collider Experiment” (ALICE), all addressing different issues in particle physics. These vertex detectors surround an interaction region between the two beams and are subjected to the intense radiation environments generated by the collisions; since the interaction region is imaged directly there is no opportunity to shield the sensors and front-end processing electronics. In addition, the acceleration and deflection magnet environments have their own set of radiation environments, in which the beam interacts with gases and materials. Collisions between the proton beam and residual gas molecules in the vacuum beam line are responsible for a large percentage of the radiation environment in these locations. The radiation environment varies greatly with location, but maximum levels can range as high as $5 \times 10^5 \text{ rad(Si)}$ (5000 Gy) ionizing dose and $1 \times 10^{14} \text{ n/cm}^2$ per year in some limited areas. Many areas have significant muon fluences as well; this negatively charged particle has approximately 200 times the mass

of an electron, is only produced in high-energy nuclear interactions and has a relatively high lifetime of $2.2\text{ }\mu\text{s}$, which renders it very penetrative. Muon effects are an issue in high-energy physics but also play an emerging role in atmospheric SEE in electronics. The diversity of radiation environments at LHC is huge, and electronic components used range from COTS parts to specifically designed radiation-hardened parts.

2.8 Summary and Closing Comments

This chapter examined the atomic sources of radiation through a review of some basic nuclear physics. This included the sources of X-rays as well as X-ray absorption. Also covered were basic and historical models of the nucleus that provided context for following sections about alpha and beta decay. Various radiation environments were also discussed, including natural radioactivity, space, nuclear reactors, nuclear weapons, and high-energy physics facilities. The discussion of natural radioactivity introduced the idea of exponential decay and the four decay series. The space environment includes discussion of solar radiation, cosmic rays, and the radiation belts, as well as atmospheric neutrons. Aspects of the nuclear reactor environment were discussed, including basic fission reaction concepts. Finally a brief discussion was provided about the nuclear weapon and high-energy physics facility environments.

Problems

2.1 Characteristic X-rays

The wavelength of the characteristic line for a given electron transition and element is given by Moseley's law

$$\sqrt{f} = k_1(Z - k_2) \quad (2.42)$$

where k_1 and k_2 are constants.

- Derive Moseley's law from Bohr's formula (Eq. (1.2)). Assume that the brightest spectral line (K-alpha) is from an L- to K-shell transition and substitute $Z - 1$ for Z . Why is the substitution of $Z - 1$ for Z reasonable?
- Moseley's law indicates that heavier elements will produce characteristic radiation with shorter wavelengths. Discuss the suitability of the various elements in Table 2.1 as well as other elements for use as X-ray anodes.

2.2 Absorption

- An X-ray source produces a continuous spectrum of radiation (due to bremsstrahlung) up to about 75 MeV. There is thick lead shielding used as protection against stray radiation. What is the most likely frequency (highest relative intensity) of radiation to be detected when testing the shielding for stray radiation?
- After an examination of Figure 2.6 one might be tempted to state that lead is about 100 times more effective than silicon at attenuating 100 keV X-rays. Is this correct?
- According to Figure 2.6, as photon energy increases, the attenuation in lead and silicon decreases. Why is this?

2.3 Liquid Drop Model

For the following liquid drop model problems, use the nuclear radius given by the Fermi model (Eq. (2.4)).

- a) Derive the surface energy term in the liquid drop model.
- b) Derive the Coulomb energy term in the liquid drop model.

2.4 The Fermi Gas Model

- a) Calculate the average nucleon energy in the Fermi gas model.

2.5 The Shell Model

- a) Derive the spin-orbit interaction dependence on l .

2.6 Alpha Decay

- a) Li^6 has an average binding energy that is less than He^4 (see Figure 2.8) so why doesn't Li^6 undergo spontaneous alpha decay?

2.7 Natural Radioactivity

- a) Elements from three of the decay series are found in nature but only the last few elements from the Neptunian series can be found in nature. Why is this?

2.8 Radiation Environments

Discuss the electronic design challenges for the various radiation environments introduced in Chapter 2.

- a) Are some environments more challenging to electronic design?
- b) Total hardness will often be a combination of shielding, radiation hardening (IC process), and circuitry redundancy. Discuss the effectiveness of each for the various types of radiation as well as how the various radiation environments may influence tradeoffs in total hardness design.
- c) Some radiation environments are not available to the designer (e.g. space and nuclear weapons environments). Discuss the various ways that radiation environments could be simulated using available resources such as radioactive elements, linear accelerators, etc.

References

There is a robust literature on radiation environments and radiation testing. It is not our objective to provide an exhaustive set of references, which in any case would take up entirely too much space. We have provided a representative set of references that are of historical interest or provide a good starting point for further study. The IEEE Transactions on Nuclear Science are the journal of record in America and include the conference proceedings for the two leading radiation effects conferences, the IEEE Nuclear and Space Radiation Effects Conference (NSREC) and its European counterpart, the [conference on] Radiations et ses Effets sur Composants et Systèmes (RADECS). The Short Courses presented at each of these conferences are an excellent resource as well.

- 1 Williams, G.P. (2009). Electron binding energies. In: *X-Ray Data Booklet*, 3e (ed. A.C. Thompson), 1-2–1-7. Berkeley, CA Table 1-1: Lawrence Berkeley National Laboratory, University of California.
- 2 Hubbell, J.H. and Seltzer, S.M. (2004). *Tables of X-Ray Mass Attenuation Coefficients and Mass Energy-Absorption Coefficients* (version 1.4), <http://physics.nist.gov/xaamdi> (accessed 18 Aug 2017). Gaithersburg, MD: National Institute of Standards and Technology.
- 3 Kramida, A., Ralchenko, Y., Reader, J., and NIST ASD Team (2018). *NIST Atomic Spectra Database* (ver. 5.5.6), <http://physics.nist.gov/asd> (accessed 19 April 2018). Gaithersburg, MD: National Institute of Standards and Technology.
- 4 Stuewer, R.H. (1997). Gamow, alpha decay, and the liquid-drop model of the nucleus. In: *George Gamov Symposium, ASP Conference Series*, vol. 129 (eds. E. Harper, W. Parke and D. Anderson), 29–43.
- 5 Evans, R.D. (1955). *The Atomic Nucleus*. New York: McGraw-Hill.
- 6 Bohr, N. (1937). Transmutations of atomic nuclei. *Science* 86 (2225): 161–165.
- 7 Bethe, H.A. and Bacher, R.F. (1936). Nuclear physics A. stationary states of nuclei. *Reviews of Modern Physics* 8: 82–229.
- 8 Fermi, E. (1946). A Course in Neutron Physics. Los Alamos Document LADC-255. Notes by I. Halpern on Los Alamos lecture series on neutron physics.
- 9 Fermi, E. (1950). *Nuclear Physics*. Notes compiled by J. Orear, A.H. Rosenfeld, and R.A. Schluter. Chicago: University of Chicago Press.
- 10 Daley, C. (2004). An improved mass formula. B.Sc. thesis. University of Surrey.
- 11 Feenberg, E. (1939). On the shape and stability of heavy nuclei. *Physics Review* 55 (5): 504.
- 12 Bohr, N. and Wheeler, J.A. (1939). The mechanism of nuclear fission. *Physics Review* 56 (5): 426.
- 13 Feenberg, E. (1947). Semi-empirical theory of the nuclear energy surface. *Reviews of Modern Physics* 19: 239.
- 14 Green, A.E.S. (1954). Coulomb radius constant from nuclear masses. *Physics Review* 95: 1006.
- 15 Blatt, J.M. and Weisskopf, V.F. (1952). *Theoretical Nuclear Physics*. New York: Wiley.
- 16 Royer, G. (2012). Generalized liquid drop model and fission, fusion, alpha and cluster radioactivity and superheavy nuclei. 4th International Conference on Current Problems in Nuclear Physics and Atomic Energy. Kiev, Ukraine.
- 17 Haxel, G. B., Hedrick, J. B., and Orris, G. J. (2002). Rare earth elements – critical resources for high technology. U.S. Geological Survey Fact Sheet 087-02. <https://pubs.usgs.gov/fs/2002/fs087-02> (accessed 18 May 2017).
- 18 Meyerhof, W.E. (1967). *Elements of Nuclear Physics*. New York: McGraw-Hill.
- 19 Cohen, B.L. (1971). *Concepts of Nuclear Physics*. New York: McGraw-Hill.
- 20 Krieger, A., Blaum, K., Bissell, M.L. et al. (2012). Nuclear charge radius of ^{12}Be . *Physical Review Letters* 108: 142501.
- 21 Arima, A. and Iachello, F. (1975). Collective nuclear states as representations of a SU(6) group. *Physical Review Letters* 35: 1069–1072.
- 22 Cook, N.D. and Hayashi, T. (1997). Lattice models for quark, nuclear structure and nuclear reaction studies. *Journal of Physics G: Nuclear Physics* 23 (9): 1109.
- 23 Nasser, G.A. (2014). Body-centered-cubic (BCC) lattice model of nuclear structure. *Journal of Nuclear Physics*.

- 24 Cook, N.D., Hayashi, T., and Yoshida, N. (1999). Visualizing the atomic nucleus. *IEEE Computer Graphics and Applications* 19 (5): 54–60.
- 25 Geiger, H. and Nuttall, J.M. (1911). The ranges of the α particles from various radioactive substances and a relation between range and period of transformation. *Philosophical Magazine* 22 (130): 613–621.
- 26 Carrington, R.C. (1859). Description of a singular appearance seen in the Sun on September 1, 1859. *Monthly Notices of the Royal Astronomical Society* 20: 13–15.
- 27 Stassinopoulos, E.G. and Raymond, J.P. (1988). The space radiation environment for electronics. *Proceedings of the IEEE* 76 (11): 1423–1442.
- 28 Barraclough, D.R., Harwood, R.M., Leaton, B.R., and Malin, S.R.C. (1975). A model of the geomagnetic field at epoch 1975. *Geophysical Journal of the Royal Astronomical Society* 43: 645–659.
- 29 Stassinopoulos, E.G. and Staffer, C.A. (2007). *Forty-Year “Drift” and Change of the SAA*. Greenbelt, MD: NASA Goddard Space Flight Center.
- 30 Fillius, R.W. and McIlwain, C.E. (1974). Measurements of the Jovian radiation belts. *Journal of Geophysical Research* 79 (25): 3589–3599.
- 31 Teague, M. J. and Stassinopoulos, E. G., (1971). A model of the Starfish flux in the inner radiation zone. *NASA/GSFC report X-601-72-487*.
- 32 Gussenhoven, M.S., Mullen, E.G., and Brautigam, D.H. (1996). Improved understanding of the Earth’s radiation belts from the CRRES satellite. *IEEE Transactions on Nuclear Science* 43 (2): 353–368.
- 33 Sawyer, D.M. and Vette, J.I. (1976). *AP-8 Trapped Proton Environment for Solar Maximum and Solar Minimum*. NASA report NASA-TM-X-72605, NSSDC/WDC-A-R/S-76-06, . Greenbelt, MD: NASA/Goddard Space Flight Center.
- 34 Vette, J.I. (1991). *The AE-8 Trapped Electron Model Environment*. NASA report NSSDC/WDC-A-R/S-91-24, . Greenbelt, MD: NASA/Goddard Space Flight Center.
- 35 Weller, R.A., Mendenhall, M.H., Reed, R.A. et al. (2010). Monte Carlo simulation of radiation effects in microelectronics. In: *IEEE Nuclear Science Symposium Conference Record, Nuclear Science Symposium*, 1262–1268. IEEE.
- 36 Swordy, S. (2001). The energy spectra and anisotropies of cosmic rays. *Space Science Reviews* 99: 85–94.
- 37 Tanabashi, M., Hagiwara, K., Hikasa, K. et al. (Particle Data Group) (2018). Review of particle physics. *Physical Review D* 98 (030001): 447.
- 38 Mewaldt, R.A. (1988). Elemental composition and energy spectra of galactic cosmic rays. In: *Proc. of Conf. on Interplanetary Particle Environment*, JPL Publication 88-28, 121–132.
- 39 Binns, W.R., Fickle, R., Waddington, C.J. et al. (1981). The heavy nuclei experiment on HEAO-3. *Proceedings of the International Astronomical Union* 94: 91–92.
- 40 Morrison, P., Olbert, S., and Rossi, B. (1954). The origin of cosmic rays. *Physics Review* 94: 440.
- 41 Ginsburg, V.L. and Pluskin, V.S. (1976). On the origin of cosmic rays: some problems in high-energy astrophysics. *Reviews of Modern Physics* 48: 161.
- 42 Gordon, M.S., Goldhagen, P., Rodbell, K.P. et al. (2004). Measurement of the flux and energy spectrum of cosmic-ray induced neutrons on the ground. *IEEE Transactions on Nuclear Science* 51 (6): 3427–3434.

- 43 Taber, A.H. and Normand, E. (1995). *Investigation and Characterization of SEU Effects and Hardening Strategies in Avionics*, Report No. DNA-TR-94-123. Alexandria, VA: Defense Nuclear Agency.
- 44 Johnson, C.W. and Holloway, C.M. (2007). The dangers of failure masking in fault-tolerant software: aspects of a recent in-flight upset event. In: *2007 2nd Institution of Engineering and Technology International Conference on System Safety*, 60–65. London.
- 45 Glasstone, S. (1955). *Principles of Nuclear Reactor Engineering*. New York: van Nostrand.
- 46 Madland, D.G. (1982). *New Fission Neutron Spectrum Representation for ENDF*, Technical Report LA-9285-MS. Los Alamos National Laboratory, DOE.
- 47 Johnson, R.T. Jr., Thome, F.V., and Craft, C.M. (1983). A survey of aging of electronics with application to nuclear power plant instrumentation. *IEEE Transactions on Nuclear Science* 30 (6): 4358–4362.
- 48 Glasstone, S. and Dolan, P.J. (eds.) (1977). *The Effects of Nuclear Weapons*. Washington, D.C.: United States Department of Defense and the Energy Research and Development Administration.
- 49 Messenger, G.C. and Ash, M.S. (1986). *The Effects of Radiation on Electronic Systems*. New York: Van Nostrand Reinhold Company.
- 50 Brode, H.L. (1969). Close-in weapon phenomena. *Annual Review of Nuclear Science* 8: 153–202.
- 51 Gover, J. E., Johnston, A. H., Halpin, J. and Rudie, N. J. (1980). Radiation effects and systems hardening. IEEE Nuclear and Space Radiation Effects Conference (NSREC) Short Course.
- 52 Srour, J. R., Longmire, C. L., Raymond, J. P. and Allen, D. J. (1982). Radiation effects and systems hardening. IEEE Nuclear and Space Radiation Effects Conference (NSREC) Short Course.
- 53 Gover, J. E., Rose, M. A., Tigner, J. E. et al. (1984). Radiation effects and systems hardening. IEEE Nuclear and Space Radiation Effects Conference (NSREC) Short Course.
- 54 van Lint, V.A.J. (1987). The physics of radiation damage in particle detectors. *Nuclear Instruments and Methods in Physics Research Section A: Accelerators, Spectrometers, Detectors and Associated Equipment* 253 (3): 453–459.